Intercomparison of large-eddy simulations of Arctic mixed-phase clouds: Importance of ice size distribution assumptions

Mikhail Ovchinnikov[1], Andrew S. Ackerman[2], Alexander Avramov[3], Anning Cheng[4], Jiwen Fan[1], Ann M. Fridlind[2], Steven Ghan[1], Jerry Harrington[5], Corinna Hoose[6], Alexei Korolev[7], Greg M. McFarquhar[8], Hugh Morrison[9], Marco Paukert[6], Julien Savre[10], Ben J. Shipway[11], Matthew D. Shupe[12], Amy Solomon[12], and Kara Sulia[13]

[1]Pacific Northwest National Laboratory, Richland, Washington, USA, [2]NASA Goddard Institute for Space Studies, New York, New York, USA, [3]Center for Global Change Science, Massachusetts Institute of Technology, Cambridge, Massachusetts, USA, [4]Science Systems and Applications Inc./NASA LaRC, Hampton, Virginia, USA, [5]Department of Meteorology, Pennsylvania State University, University Park, State College, Pennsylvania, USA, [6]Karlsruhe Institute of Technology, Karlsruhe, Germany, [7]Environment Canada, Toronto, Ontario, Canada, [8]Department of Atmospheric Sciences, University of Illinois at Urbana-Champaign, Urbana, Illinois, USA, [9]National Center for Atmospheric Research, Boulder, Colorado, USA, [10]Department of Meteorology, Stockholm University, Stockholm, Sweden, [11]Met Office, Exeter, UK, [12]Cooperative Institute for Research in Environmental Science, University of Colorado/NOAA, Boulder, Colorado, USA, [13]Geophysical Fluid Dynamics Laboratory, Princeton University, Princeton, New Jersey, USA

Abstract Large-eddy simulations of mixed-phase Arctic clouds by 11 different models are analyzed with the goal of improving understanding and model representation of processes controlling the evolution of these clouds. In a case based on observations from the Indirect and Semi-Direct Aerosol Campaign (ISDAC), it is found that ice number concentration, N_i, exerts significant influence on the cloud structure. Increasing N_i leads to a substantial reduction in liquid water path (LWP), in agreement with earlier studies. In contrast to previous intercomparison studies, all models here use the same ice particle properties (i.e., mass-size, mass-fall speed, and mass-capacitance relationships) and a common radiation parameterization. The constrained setup exposes the importance of ice particle size distributions (PSDs) in influencing cloud evolution. A clear separation in LWP and IWP predicted by models with bin and bulk microphysical treatments is documented and attributed primarily to the assumed shape of ice PSD used in bulk schemes. Compared to the bin schemes that explicitly predict the PSD, schemes assuming exponential ice PSD underestimate ice growth by vapor deposition and overestimate mass-weighted fall speed leading to an underprediction of IWP by a factor of two in the considered case. Sensitivity tests indicate LWP and IWP are much closer to the bin model simulations when a modified shape factor which is similar to that predicted by bin model simulation is used in bulk scheme. These results demonstrate the importance of representation of ice PSD in determining the partitioning of liquid and ice and the longevity of mixed-phase clouds.

1. Introduction

Low-level Arctic clouds receive much attention because of their ubiquity and potentially important role in the sensitive and rapidly changing Arctic climate. Multiple field programs [*McFarquhar et al.*, 2011; *Uttal et al.*, 2002; *Verlinde et al.*, 2007] and numerous theoretical and modeling studies [e.g., *Morrison et al.*, 2012 and references therein] have expanded our knowledge of these clouds' properties and formation mechanisms. Yet climate models continue to struggle with simulating these clouds realistically, partly because cloud layers in the Arctic are often thin and challenging to resolve in coarse-resolution models, and partly because our understanding of their governing processes is still incomplete. Many remaining gaps are related to predicting the phase of cloud and precipitation particles as ice processes become active at temperatures below freezing, a condition particularly common at higher latitudes. Accurate prediction of cloud phase is especially important for persistent mixed-phase cloud layers because their very existence hinges on the correct liquid-to-ice condensate partitioning. Excessive ice formation can diminish the liquid phase, which is largely responsible for the cloud top radiative cooling that drives circulations necessary to sustain the cloud.

High-resolution cloud modeling, including large-eddy simulation (LES), is increasingly used to develop and test cloud parameterizations for large-scale models. With respect to mixed-phase clouds, this strategy is complicated by the fact that the range of cloud properties from different LES models is often too wide to provide a reliable reference solution that can be used to gauge parameterization performance. It is therefore important to understand the sources of inter-model differences not only in cloud properties simulated under specified conditions but also in responses of simulated clouds to variations in input parameters, such as ice nucleus concentration. This study is aimed at gaining such understanding.

Two recent model intercomparisons focusing on single-layer mixed-phase Arctic clouds provide a context for this activity. An intercomparison based on the Mixed-Phase Arctic Cloud Experiment (MPACE) documented a large spread of model results in simulations of a single-layer mixed-phase cloud during the Arctic fall [*Klein et al.*, 2009]. Models differed widely in simulated properties of a cloud layer formed over open ocean with large surface turbulent heat fluxes, variable cloud top temperatures around $-15°$C, and low aerosol number concentrations. Liquid water path (LWP) and ice water path (IWP) values from several cloud-resolving models were scattered across 2 orders of magnitude. An even wider range of results was obtained when single-column models were included. Perhaps the most striking differences were found in ice number concentration predicted by the models using available ice nucleation parameterizations and MPACE field measurements.

In a follow-up intercomparison based on a case from the Surface Heat Budget of the Arctic Ocean (SHEBA) and First International Satellite Cloud Climatology Project (ISCCP) Regional Experiment—Arctic Clouds Experiment (FIRE-ACE) [*Morrison et al.*, 2011], the ice particle number concentration was constrained uniformly across cloud-resolving and LES models to remove an obvious source of spread in the MPACE results. In this case, a well-mixed boundary layer coupled to the surface contained a persistent mixed-phase cloud that precipitated to the surface in the form of light snow. Appreciable liquid water was present despite the low temperature ($-20°$C near cloud top)—a feature reproduced by most models. Although a number of simulations exhibited a qualitatively similar behavior, the range of predicted LWP and IWP was still large, despite the constrained ice number concentrations. When the prescribed ice particle number concentration (N_i) was varied, simulations revealed pronounced model sensitivities, such that the larger ice deposition rates associated with increased N_i initiated a number of dynamical and radiative feedbacks that led to dissipation of liquid. In most models, clouds glaciated when the deposition growth rate of cloud ice exceeded 2×10^{-5} g m^{-3} s^{-1}. In a study of the same case using prognostic ice nuclei, *Fridlind et al.* [2012b] concluded that LWP was weakly desiccated by the observed ice, consistent with efficient consumption of ice nuclei and a long-lived mixed-phase state.

Results of the SHEBA model intercomparison [*Morrison et al.*, 2011] indicate that a factor of two differences in ice depositional growth rates inside the liquid cloud layer are common among different models for any given ice water content. Since the ice number concentration was constrained to be the same in all models, there are two potential sources for these differences. First, different ice crystal shapes, or habits, could lead to variations in depositional growth rate and fall speed for particles of the same mass because of corresponding changes in capacitance and drag. Alternatively, variations in depositional growth rate could be due to differences in particle size distributions (PSDs) and corresponding differences in the size distribution moments. Understanding the sources of these differences is important to both improving high-resolution process-oriented models and guiding the development of parameterized representations of ice-containing clouds in large-scale models. Simulations performed for the present intercomparison are designed to investigate the origins of the diversity among model results with regard to these ice properties. Specifically in the case described below, mass-size, capacitance-mass, and fall speed-size relationships are prescribed, so that the rates for depositional growth and sedimentation are constrained across different models. A simple parameterization for the longwave radiative cooling rate is also formulated to eliminate another potentially important source of inter-model variability. These features of the setup isolate differences due to model physics. Finally, all models use identical horizontal and comparable vertical grids thereby excluding the effects of spatial resolution that likely contributed to the divergence of results in previous intercomparisons.

The rest of the paper is organized as follows. Our modeling approach is described in section 2.. Section 3. focuses on the time evolution of the cloud layer and liquid-to-ice partitioning simulated by different models, while section 4. focuses on the role of unconstrained aspects of ice microphysics. Insights gained and broader implications of the presented findings are discussed in section 5.. Finally, section 6. summarizes the key results of the study.

Table 1. Models Participating in the Intercomparison

Model	Developer/User	Reference	Microphysics[a]
COSMO	Karlsruhe Institute of Technology, Germany	*Vogel et al.* [2009]	Bulk 2M[b] [*Seifert and Beheng*, 2006]
DHARMA-bin	NASA GISS, USA	*Fridlind et al.* [2012b]	Bin [*Fridlind et al.*, 2012b]
DHARMA-2M	NASA GISS, USA	*Fridlind et al.* [2012a]	Bulk 2M [*Morrison et al.*, 2005]
METO	Met Office, UK	*Shutts and Gray* [1994]	Bulk 2M[b] [*Ferrier*, 1994]
RAMS	Penn State, USA	*Cotton et al.* [2003]	Bulk 2M[b] [*Meyers et al.*, 1997]
SAM-bin	PNNL, USA	*Fan et al.* [2009] and *Khairoutdinov and Randall* [2003]	Bin [*Khain et al.*, 2004]
SAM-2M	PNNL, USA	*Khairoutdinov and Randall* [2003]	Bulk 2M [*Morrison et al.*, 2005]
UCLALES	NASA Langley, USA	*Stevens et al.* [2005]	Bulk 2M [*Morrison et al.*, 2005]
UCLALES-SB	Stockholm University, Sweden	*Stevens et al.* [2005]	Bulk 2M[b] [*Seifert and Beheng*, 2006]
WRFLES	University of Colorado/NOAA, USA	*Yamaguchi and Feingold* [2012]	Bulk 2M [*Morrison et al.*, 2005]
WRFLES-PSU	Penn State, USA	*Yamaguchi and Feingold* [2012]	Bulk 2M[b]

[a]All microphysics schemes are modified according to the specifications described in this section and the Appendix .
[b]Droplet number concentration is fixed in the submitted simulations, making liquid-phase microphysics a one-moment scheme.

2. Approach

The case is derived from an extended mixed-phase stratiform Arctic cloud deck observed on 26 April 2008 during the Indirect and Semi-Direct Aerosol Campaign (ISDAC) [*McFarquhar et al.*, 2011]. On this day, a high-pressure system was present over the North Pole and a stratiform cloud deck formed in a mixed layer decoupled from the surface layer over the thin sea ice north of Barrow, Alaska and persisted for 15 h [*Jackson et al.*, 2012]. Conditions observed on that day are relatively well suited for designing a semi-idealized modeling case and for developing conceptual understanding of several interacting processes. Microphysically, the majority of observed ice particles were pristine dendrite crystals although some ice aggregation may have occurred. Drizzle and riming, which complicated the MPACE case, were absent. The single-layer nature of the cloud ensures that there are no complications of a seeder-feeder mechanism from ice falling from above the liquid layer. Dynamically, the decoupled cloud layer differs from the coupled boundary layers in the MPACE and SHEBA single-layer cases.

The case is simulated by 11 different model configurations listed in Table 1. Nine configurations employ two-moment (2M) bulk microphysics parameterizations in which mass and number mixing ratios for liquid and ice hydrometeors are predicted using assumed shapes of the PSDs. Two configurations, DHARMA-bin and SAM-bin, use a size-resolved (bin) treatment of microphysics, which explicitly predicts the discretized PSDs. Four frameworks (DHARMA, SAM, UCLALES, and WRFLES) are coupled to two different microphysics schemes each. A microphysics scheme based on *Morrison et al.* [2005] is coupled to four different dynamical cores (DHARMA-2M, SAM-2M, UCLALES, and WRFLES), while a scheme based on *Seifert and Beheng* [2006] is used in two models (COSMO and UCLALES-SB). This variety of model configurations helps to more robustly determine whether differences among the simulations are attributable to the treatment of dynamical or microphysical aspects.

2.1. Case Description and Simulation Setup

All simulations are performed on a three-dimensional domain. Horizontal model grid spacing is 50 m and vertical grid spacing is 10 m below a 1200 m level. Above this level, the vertical grid spacing is allowed to vary but has negligible impact on the evolution of the cloud confined to the lower 850 m. The model domain extends at least 3.2 km (64 grid points) in both horizontal directions and 1.5 km in the vertical.

The model is initialized with vertical profiles of temperature, moisture, and horizontal wind components shown in Figure 1. Detailed specifications of the initial and boundary conditions for the case are given in the Appendix A.

To minimize inter-model differences due to radiative transfer codes, all models parameterize the longwave radiative cooling as a function of the liquid water content (LWC) profile, an approach adopted in several previous GEWEX cloud system study (GCSS) intercomparison projects [e.g., *Ackerman et al.*, 2009; *Stevens et al.*, 2005] and evaluated in *Larson et al.* [2007]. The parameterization details are described in the Appendix A. Shortwave radiation is neglected.
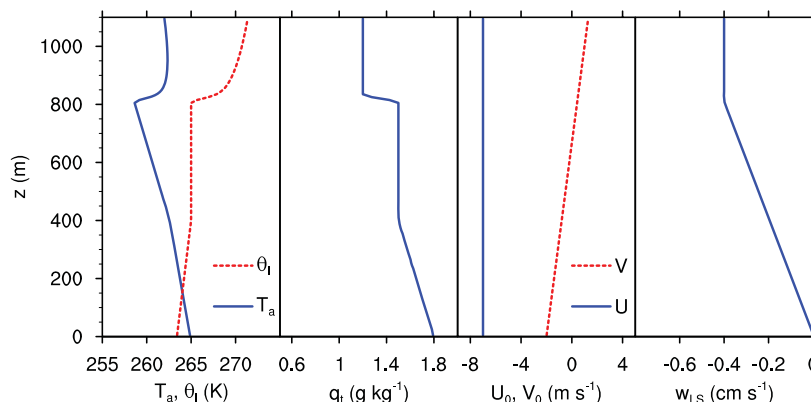
Figure 1. Initial profiles of absolute (T_a) and liquid water potential (θ_l) temperatures, total water mixing ratio (q_t), horizontal wind components (U, V), and large-scale subsidence (w_{LS}).

Each model performs three simulations with different target ice number concentrations, N_{i0}, listed in Table 2. A method of enforcing N_{i0} is described in section 2.3.. Additional sensitivity runs are conducted using several models as will be presented later. In all simulations, ice processes are excluded in the first 2 h to allow the mixed-layer turbulence to develop. After this spin-up, the models are run for six more hours (for a total length of each simulation of 8 h) using the specified N_{i0}. The baseline N_{i0} in the ice1 simulation (1 L^{-1}) is selected to approximate in-cloud ice crystal number concentrations based on multiple measurements during ISDAC [*McFarquhar et al.*, 2011; *Fan et al.*, 2011]. The minimum N_{i0} of zero represents pure liquid-phase clouds with no ice. The maximum N_{i0} (4 L^{-1}) represents a multiple of the observation-derived baseline that could reasonably result from increasing ice nucleus number concentration, which may vary by orders of magnitude [*DeMott et al.*, 2010].

2.2. Liquid-Phase Microphysics

Since the cloud observed during 26 April had a nearly constant droplet number concentration (N_d) [*Fan et al.*, 2011; *McFarquhar et al.*, 2011; *Zelenyuk et al.*, 2010], a value of $N_d = 200$ cm^{-3} is specified in models that prescribe droplet number concentration. In models with a prognostic droplet number concentrations option, a cloud condensation nucleus (CCN) size distribution is given as a sum of two lognormal aerosol size distributions for accumulation and coarse modes with concentrations of 207 and 8.5 cm^{-3}, modal diameter of 0.2 and 0.7 μm, and geometric standard deviation of 1.5 and 2.45, respectively. These parameters provide the best fit to the measured distributions below the liquid cloud layer [*Earle et al.*, 2011].

For the droplet activation calculation, the aerosol composition is assumed to be ammonium bisulfate. According to single-particle mass spectrometry measurements taken during ISDAC, the aerosol chemical composition was complex and most particles contained a significant fraction of organic compounds [*Zelenyuk et al.*, 2010]. However, the aerosol number size distribution peaks at a relatively large diameter of 0.2 μm, and the majority of CCN activates into droplets at low supersaturation (at or below $S_w = 0.15\%$) for a reasonable range of aerosol composition assumptions. Because such supersaturations can easily be generated even by slow updrafts, the sensitivity of droplet number concentration to aerosol composition in this case is found to be weak.

Drizzle was essentially absent in observations of the studied cloud, which is consistent with drizzle formation being inhibited by a relatively small LWC (~0.2 g m^{-3}) and a droplet concentration that is not low (~200 cm^{-3}) [*Comstock et al.*, 2004]. Thus, for simplicity, all models are run with the collision-coalescence process turned off.

Table 2. Simulations Performed With Each Model

Case	Description
ice0	Liquid-only case, no ice $N_{i0} = 0$ L^{-1}
ice1	Target ice concentration (equation (1)) $N_{i0} = 1$ L^{-1}
ice4	Target ice concentration (equation (1)) $N_{i0} = 4$ L^{-1}

2.3. Ice-Phase Microphysics

The precise mechanisms of ice initiation in the atmosphere remain poorly understood [*Koop*, 2013]. Even when an airborne instrument is dedicated to measuring ice nucleus number concentrations as a function of temperature and relative

humidity, as in this case [*McFarquhar et al.*, 2011], the measurements remain insufficient to fully constrain model schemes [cf. *Fridlind et al.*, 2012b]. To test the sensitivity of the structure of the mixed-phase cloud to ice crystal concentration without speculating on the exact ice nucleation mechanisms, in this study, ice particle formation is parameterized in a simple way analogous to the formulation used in the recent intercomparison of SHEBA simulations [*Morrison et al.*, 2011]. The parameterization is designed to maintain a constant (prescribed) ice particle number mixing ratio ($N_{i,0}$) within a mixed-phase cloud. If the ice particle number in a grid point is reduced, new ice crystals are formed to bring ice concentration to $N_{i,0}$, provided that the ice supersaturation exceeds 5% and the grid point contains liquid water. Following *Ovchinnikov et al.* [2011], the latter condition is introduced to exclude ice nucleation in the deposition mode, which is thought to be ineffective in the considered temperature range ($-11°C$ to $-15°C$) [*Hoose and Möhler*, 2012].

Thus, the ice nucleation rate is given by

$$
\begin{aligned}
\frac{\partial N_i}{\partial t} &= \max\left(0, \frac{N_{i0} - N_i}{\Delta t}\right), \quad S_i \geq 0.05 \text{ or } q_l \geq 0.001 \text{ g kg}^{-1} \\
\frac{\partial N_i}{\partial t} &= 0, \quad\quad\quad\quad\quad\quad S_i < 0.05 \text{ or } q_l < 0.001 \text{ g kg}^{-1}
\end{aligned}
\tag{1}
$$

where N_{i0} is the target ice particle concentration discussed below, N_i is the model predicted ice concentration, Δt is the model time step, S_i is the fractional supersaturation over ice, and q_l is the liquid water mixing ratio.

Once formed, ice crystals are subjected to diffusional growth and sublimation, gravitational settling, resolved advection, and subgrid-scale mixing. In the simulations analyzed here, ice particles grow only through water vapor deposition. (Though average ice crystal size can change from sedimentation-induced size sorting.) Riming and aggregation are turned off. This simplifying approximation is consistent with observations being dominated by unrimed and unaggregated dendrite crystals [*Lawson*, 2011]. It must be noted, however, that aggregates can be important in Arctic stratiform clouds [e.g., *Avramov et al.*, 2011] and their role is worth exploring in future studies.

A unique feature of this intercomparison is that all participating models were modified to use the same ice particle properties, including specified relationships among mass, crystal diameter, capacitance, and fall speed, as described in the Appendix .

3. Structure of the Mixed-Phase Cloud

3.1. Vertical Structure

To set the stage for the analysis of inter-model differences and sensitivity of simulations to N_{i0}, essential features of the cloud evolution are first described using the SAM-2M ice1 simulation as an illustrative example.

Liquid-phase cloud is formed immediately within a saturated part of the profile (Figure 2a). Cloud top radiative cooling leads to formation of negatively buoyant air in the upper part of the cloud and consequently to the generation of turbulent motions and a cloud-driven mixed layer. Within the first 30 min, the layer between 400 and 800 m becomes turbulent, as evident from the increasing vertical velocity variance (Figure 2c). The turbulent mixed layer continues to deepen downward by entraining moisture from below and deepening the liquid-phase cloud. The base of the mixed layer reaches the surface after about 5 h. At this point the model enters a quasi steady state regime, when cloud properties do not change much. We note that throughout the simulations the cloud top height is nearly constant, indicating that the cloud top entrainment is nearly balanced by the prescribed large-scale subsidence.

Following the outlined setup specifications, ice is allowed to form at 2 h into the simulation (Figure 2b). By design, the ice crystal number concentration within the liquid cloud immediately reaches the value prescribed for the experiment. Once formed, ice particles begin to populate the subcloud layer, being transported there by downdrafts, subgrid-scale diffusion, and sedimentation. Precipitating ice particles first reach the surface shortly before $t = 3$ h (Figure 2b). Quasi steady state cloud property profiles developed after about 5 h are very similar to those described in detail by *Ovchinnikov et al.* [2011]. Simulations by other
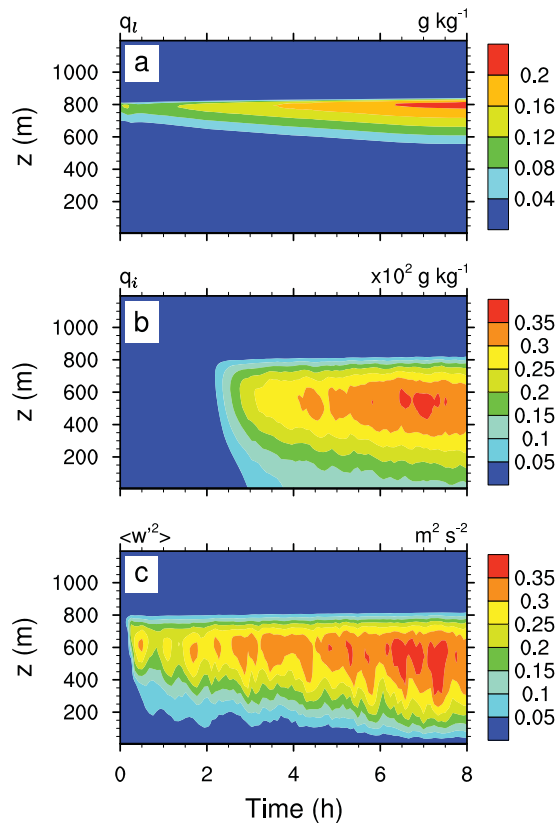
Figure 2. Time evolution of the domain-mean profiles of (a) liquid water and (b) ice mixing ratios, and (c) vertical velocity variance from the SAM-2M ice1 simulation.

models exhibit similar main features of cloud evolution, although quantitative differences occur as discussed below.

3.2. Time Series Comparison

An important characteristic of a mixed-phase cloud is the partitioning of condensate between liquid and ice. We first consider this partitioning in terms of liquid and ice water paths (LWP and IWP, respectively), which represent horizontally averaged and vertically integrated amounts of liquid and ice water in a model domain. Time evolutions of LWP and IWP for three runs from all models are shown in Figure 3. In simulations without ice (ice0), the LWP increases nearly linearly after the initial half-an-hour spin-up during which the turbulent motions develop. This increase is due to the downward expansion of the mixed layer by entraining the moister air below 400 m (cf. Figure 1). Once the mixed layer extends all the way to the surface, the LWP stabilizes. This evolution pattern is common to all models, although the rates of LWP increase vary among models. Because of the differences in the circulation strengths, the time needed for the mixed layer to extend to the surface and for the LWP to level off ranges from 4.5 to 7 h. Slow increases in LWP after the models reach this quasi-steady state is likely due to reduction in temperature

caused by continuous radiative cooling. For ice0 simulations, the LWP values are within about 10% of each other at the end of the eighth hour, although the differences can be as large as 50% at earlier times. Notably, the differences among models using the same microphysics (e.g., DHARMA-2M, SAM-2M, UCLALES, and WRFLES) are larger than the differences between simulations using the same dynamical core but different microphysics schemes (cf. bin and 2M simulations for DHARMA and SAM). Thus, although microphysical schemes contribute to the inter-model range in LWP, the spread appears to be dominated by differences in physical or numerical representations of other processes, such as advection, subgrid mixing, etc. The lack of model agreement in predicted mixed-layer-base descent rates even for ice0 simulations indicates that decoupled cloudy boundary layers do present some challenge even for relatively high-resolution LES.

When ice is allowed to form, water vapor mixing ratios are reduced, and the LWP is expected to be lower than in the simulations without ice. This is indeed the case for ice1 and ice4 simulations, in which LWP is reduced on average by 7 and 25 g m^{-2}, respectively, at the end of simulations compared to ice0 (Figures 4a and 4c). The LWP reduction relative to ice0 is seen across all models, but the change is not uniform. In fact, the inter-model differences in ice-induced changes in LWP in ice1 runs (Figure 4a) are comparable to the spread of LWP in ice0 simulations (Figure 3a), while for the ice4 simulations the differences are several times larger (Figure 4c). Thus, while the LWP range in ice0 simulations is attributable primarily to the differences in formulation of model dynamics (e.g., advection, mixing, and entrainment), the ice-induced changes appear to be caused by microphysics and its coupling with the dynamics. Larger ice concentrations have a stronger impact on cloud evolution. In ice1 simulations, LWP evolution is qualitatively similar to ice0 (Figure 3b), but in ice4 simulations the LWPs predicted by different models continue to diverge into three distinct groups: high, medium, and low LWP (Figure 3d). As will be shown below, this grouping results from differences in microphysical assumptions.
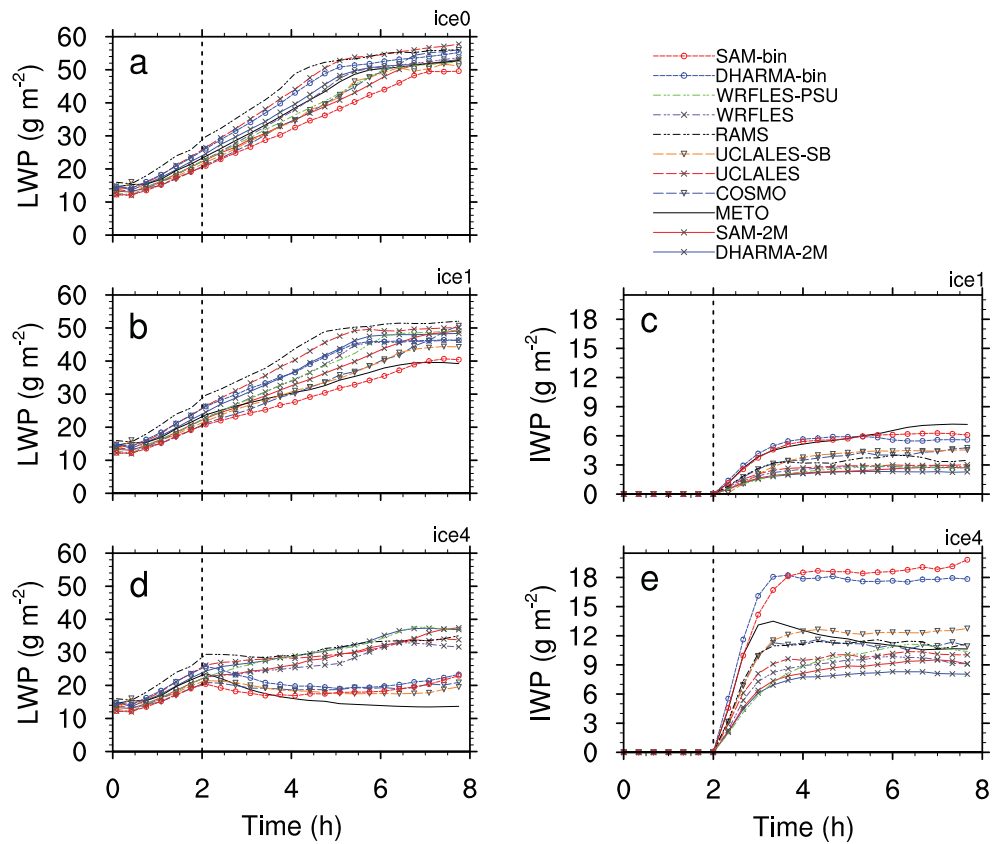
Figure 3. Time evolution of the (a, b, and d) domain mean liquid and (c and e) ice water paths for ice0 (Figure 3a), ice1 (Figures 3b and 3c), and ice4 (Figures 3d and 3e) simulations. The vertical dashed line indicates time when ice processes are turned on. Simulations are marked with crosses for *Morrison et al.* [2005] microphysics, triangles for *Seifert and Beheng* [2006] microphysics, and circles for bin microphysics schemes.

The LWP reduction in ice-containing simulations is partially compensated by an increase in IWP, such that the total condensed (liquid + ice) water path changes less than LWP (Figure 4). In fact, IWP initially increases faster than LWP decreases, so in all models the total condensed water path rises in the first hour after
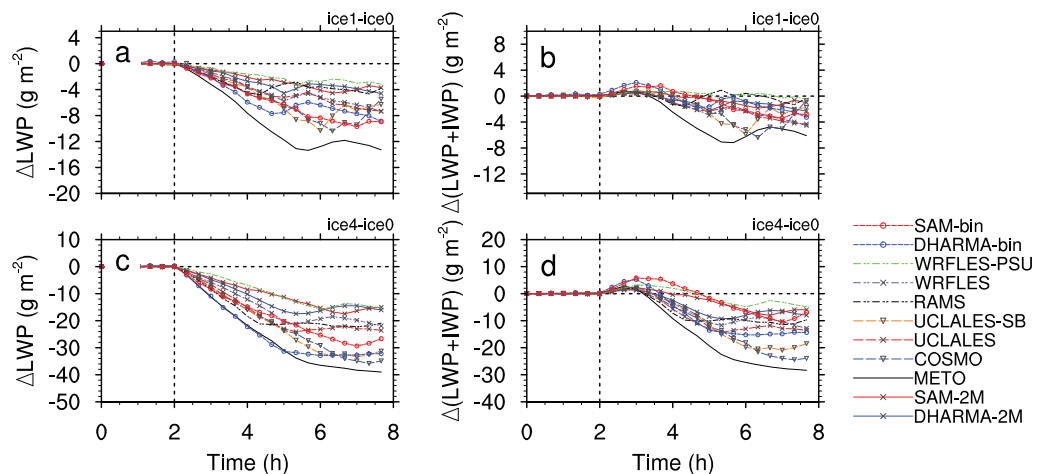

Figure 4. Time evolution of changes in (a and c) liquid and (b and d) total condensed (liquid + ice) water paths between ice1 and ice0 simulations (Figures 4a and 4b) and ice4 and ice0 simulations (Figures 4c and 4d). The vertical dashed line indicates time when ice processes are turned on. Line labels are the same as in Figure 3.
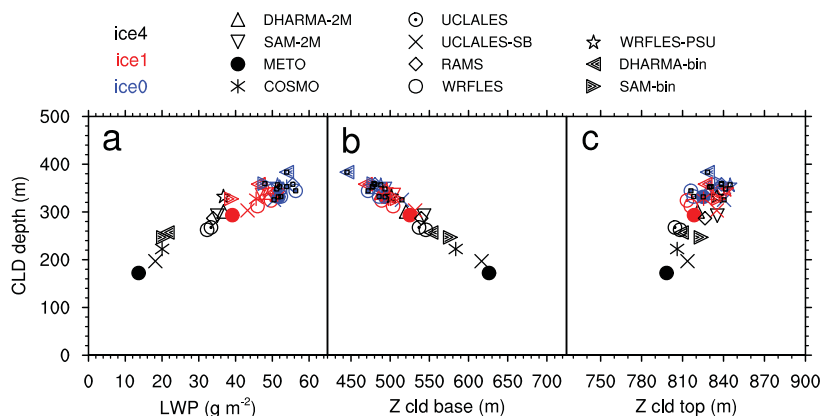
Figure 5. Scatterplots showing relation between cloud depth (CLD depth) and (a) liquid water path (LWP) and (b) altitudes of liquid cloud base (Z cld base) and (c) cloud top (Z cld top). Each symbol represents an average value for the last 2 h of simulations. The ice0 runs are shown in blue, ice1 in red, and ice4 in black.

introduction of ice (time period between 2 and 3 h, Figures 4b and 4d). Due to the difference between saturation water vapor pressures over ice and liquid, ice particles have a larger reservoir of moisture available for their growth than liquid droplets do, which initially increases the total condensate production relative to the ice0 simulations. After about an hour, however, IWP stabilizes, as precipitation balances vapor deposition on ice, while the LWP continues to deviate further from the simulations without ice. At 8 h, the mean total condensed water path decreases relative to ice0 simulations by 3 and 13 g m^{-2} in ice1 and ice4 simulations, respectively (Figures 4b and 4d), which means that IWP gains compensate only about half of the LWP loss. As will be shown later, most of that difference can be attributed to the removal of moisture by precipitating ice, but in some simulations, particularly in ice4 configuration, the feedback linking LWC, cloud top radiative cooling, and the intensity of turbulence becomes important.

All models simulate a near-adiabatic linear increase in liquid cloud water content with height. Thus, LWP is directly related to the liquid cloud depth (Figure 5a). (Cloud is defined by grid cells with $q_l > 0.01$ g kg^{-1}.) The cloud depth change, in turn, is driven primarily by the cloud base height change (Figure 5b), while the cloud top height varies relatively little (Figure 5c).

Without ice the simulated clouds do not precipitate. Low LWC (under 0.2 g m^{-3}) and a relatively high droplet number concentration (∼200 cm^{-3}) lead to small droplet sizes and inefficient collision coalescence, justifying the exclusion of this process in the simulation setup. When ice particles are allowed to form, they grow to sizes with appreciable sedimentation velocities. Removal of moisture from the mixed-phase cloud layer, as characterized by the precipitation flux at the 400 m level (Figures 6a and 6b), contributes to the reduction in LWP in ice-containing simulations relative to ice0. Above this level, the water vapor is saturated with respect to ice and ice particles grow by deposition. Below 400 m, ice particles sublimate, and the precipitation fluxes are reduced. Less than half of precipitation from 400 m (Figures 6a and 6b) reaches the surface (Figures 6c and 6d), indicating that precipitation sublimation is a source of near-surface water vapor. The inter-model spread in precipitation fluxes is analogous to that of IWP (cf. Figures 6, 3c, and 3e).

3.3. Liquid-to-Ice Partitioning and the Role of the Dynamics

Partitioning of condensate into liquid and ice in terms of time-averaged liquid and ice water paths is illustrated in Figure 7. As has been noted above, LWP and IWP are anticorrelated. Larger ice number concentration results in larger IWPs and smaller LWPs. In simulations with ice, the total condensate amount in the atmospheric column decreases relative to the ice0 simulation. This decrease, which is most pronounced for the ice4 simulations, can be understood by considering the main source and sink of the total water in the cloud topped mixed layer. The only source of moisture for the mixed layer is entrainment of humid air from below. The ability of a model to tap into that moisture reservoir depends on the strength of the circulation, which can be characterized by the standard deviation of the vertical velocity (σ_w). Figure 8a clearly illustrates a strong correlation between σ_w and the total amount of condensate (LWP + IWP), which is driven by
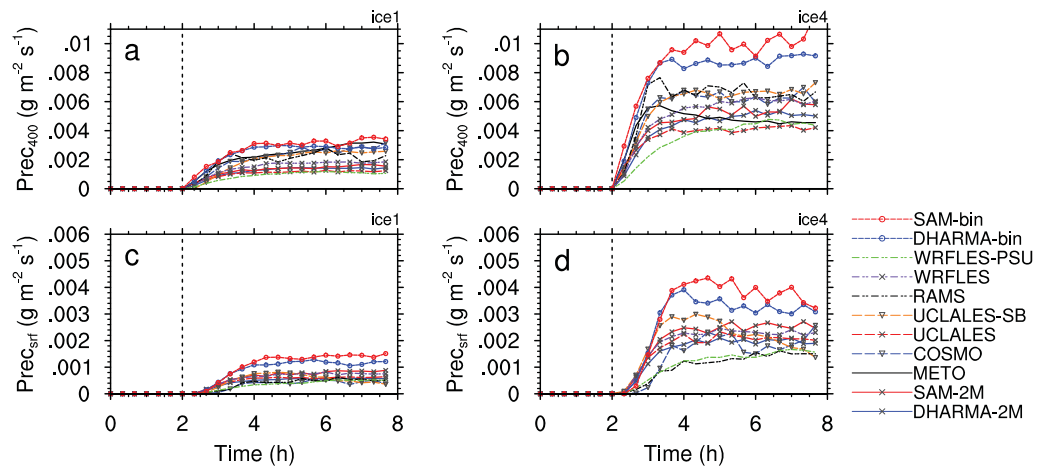
Figure 6. Time evolution of precipitation flux (a and b) at 400 m level and (c and d) at the surface. The vertical dashed line indicates time when ice processes are turned on. Line labels are the same as in Figure 3.

the LWP (Figure 8c), which in turn is strongly tied to the liquid cloud depth (Figure 8b). This correlation holds not only for runs for each model with different ice settings (same symbols of different colors in Figure 8a), but also for simulations for the same ice setting by different models (different symbols of the same color in Figure 8a). Stronger circulations entrain moisture from below more efficiently and produce mixed layers with lower base heights and thicker clouds (Figure 8b). Since larger (smaller) LWP also leads to stronger (weaker) cloud top radiative cooling, there is a positive feedback that tightens up the correlations between σ_w and LWP and between σ_w and liquid cloud depth.

A similar dependence of IWP on σ_w is not found, as evident from the large scatter of points in Figure 8d. For each model configuration, an increasing ice concentration does lead to larger IWP and smaller σ_w (Figure 8d). This is to be expected and is consistent with higher N_i and IWP leading to smaller LWP and, in particular, smaller cloud top LWC, which results in reduced radiative cooling and, consequently, weaker circulation. However, the lack of correlation between the IWP and σ_w predicted by different models for a given N_i (i.e., points shown by different symbols of the same color in Figure 8d) indicates that the spread of IWP for a given N_i is not primarily controlled by the spread of dynamics, as discussed below.

For the column of mixed-layer and near-surface air, the only significant sink of moisture is ice precipitation, since cloud top entrainment, which can also contribute to the d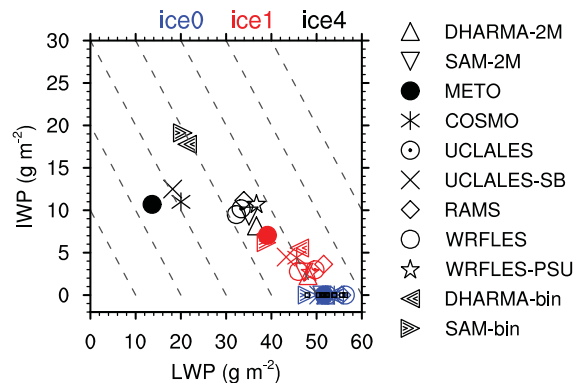rying of the mixed layer, is weak in this case. Even though the precipitation is light, during the 6 h of mixed-phase cloud evolution between 8 and 24 g m^{-2} of moisture is removed from the boundary layer in ice1 simulations and between 25 and 70 g m^{-2} in ice4 simulations.

4. Ice Microphysics Effects

In this study, the microphysical characteristics of individual ice particles are constrained and yet there remains significant variability in ice cloud properties among the models. Part of this variability comes from the differences in the dynamics and structure of the mixed layer and liquid cloud, as discussed above. There are, however, important contributions to this variability that come from
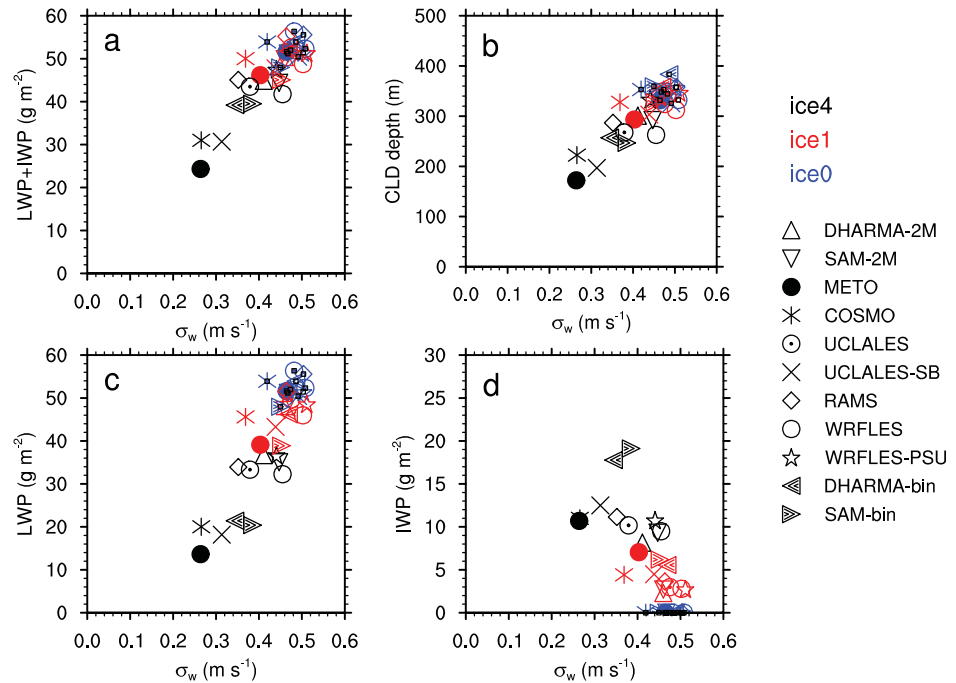

Figure 7. Liquid (LWP) and ice (IWP) water paths. Dashed lines indicate constant total (LWP+IWP) condensate amount. Each symbol represents an average value for the last 2 h of simulations. The ice0 runs are shown in blue, ice1 in red, and ice4 in black.

Figure 8. (a) Total condensed water path, (b) liquid cloud depth (CLD depth), (c) liquid water path (LWP), and (d) ice water path (IWP) versus the standard deviation of vertical velocity (w_{std}). w_{std} is computed as a square root of the mean vertical velocity variance below 950 m level. Each symbol represents an average value for the last 2 h of simulations. The ice0 runs are shown in blue, ice1 in red, and ice4 in black.

two aspects of ice microphysics not constrained by the model setup: ice PSD and changes in ice number concentration during sublimation.

4.1. Effects of Ice PSD on Bulk Process Rates

All models in this intercomparison use the same mass-size, capacitance-size, and fall speed-size relationships for ice particles. In bin microphysics schemes (DHARMA-bin and SAM-bin), these relationships control the rates for ice processes, such as depositional growth and sedimentation, in each size bin and therefore directly govern the evolution of ice PSDs. For bulk microphysics schemes, however, the shape of the ice PSD has to be specified in order to obtain the integrated process rate from individual particle properties. For example, in five models (DHARMA-2M, METO, SAM-2M, UCLALES, WRFLES, and WRFLES-PSU), ice PSD are assumed to follow a gamma distribution in the form

$$f_D(D) = A \ D^v exp(-\lambda \ D), \tag{2}$$

where D is the crystal maximum dimension, v and λ are two parameters of the distribution, $A = N_i \ \lambda^{v+1}/\Gamma(v+1)$, N_i is the total ice number concentration, and Γ is the gamma function. (Note that here maximum dimension is the same as the diameter of the prescribed ice spheres, which have a density less than one tenth that of bulk ice.) In the default configuration of the scheme used in this intercomparison, the shape parameter v is set to zero and the distribution is reduced to an exponential ice PSD [*Morrison et al.*, 2005]

$$f_D(D) = N_0 \ exp(-\lambda \ D), \tag{3}$$

where λ and N_0 are the slope and intercept parameters, respectively. Ice number concentration, N_i, and ice water content, q_i, related to the 0th and 3rd moments of the PSD, respectively, can be expressed as

$$\int_0^\infty f_D(D)dD = \frac{N_0}{\lambda} = N_i, \tag{4}$$

$$\frac{\pi}{6} \rho_i \int_0^\infty D^3 f_D(D) dD = \frac{\pi}{6} \rho_i \frac{6}{\lambda^4} \; N_0 = \frac{\pi}{\lambda^3} \; \rho_i N_i = q_i \; . \tag{5}$$

The two parameters of the PSD in equation (3) are therefore uniquely defined by N_i and q_i predicted by a two-moment microphysics scheme as

$$\lambda = \left(\pi \rho_i \; \frac{N_i}{q_i} \right)^{1/3} \text{and} \; N_0 = \lambda \; N_i. \tag{6}$$

Ice PSDs in two other models (COSMO and UCLALES-SB) are based on a modified gamma distribution (MGD) expressed in terms of ice particle mass, m, rather than size [*Seifert and Beheng*, 2006]

$$f_m(m) = A_m \; m^{v_m} exp(-\lambda_m \; m^\mu). \tag{7}$$

Noteworthy for the purpose of this intercomparison and, more generally, for any comparisons of different microphysical schemes is that the parameters of the MGD change when the distribution type changes (e.g., size versus mass) [*Petty and Huang*, 2011]. Thus, an exponential distribution in terms of D ($v = 0$ in equation (2)) becomes a MGD in terms of m with $\mu = 1/3$ and $v_m = -2/3$ [*Seifert and Beheng*, 2006]. Similarly, the default values in COSMO and UCLALES-SB ($v_m = 0$ and $\mu = 1/3$ in equation (7)) result in a gamma distribution with $v = 2$ in terms of D (equation (2)) [*Petty and Huang*, 2011]. In the following discussion, the distributions are considered in terms of ice particle diameter (D), unless stated otherwise.

The shape of the distribution is important because it affects the process rates for sedimentation, depositional growth, and sublimation of ice particles. Because these processes depend on different moments of the PSD, it is instructive to examine relationships among the moments of distributions with different shape parameters. For a gamma distribution in the form of equation (2), the moment p is given by

$$M_p = \; N_i \; \lambda^{-v} \; \Gamma(p+v+1)/\Gamma(v+1). \tag{8}$$

The ratio of any moment to the same moment of the exponential distribution (i.e., $v = 0$) is

$$\frac{M_{p,v}}{M_{p,v=0}} = \frac{\Gamma(p+v+1)}{\Gamma(p+1)\Gamma(v+1)} \left(\frac{6 \cdot \Gamma(v+1)}{\Gamma(v+4)} \right)^{p/3} . \tag{9}$$

Figure 9 illustrates how this ratio changes as a function of p and v. Because both exponential and gamma distributions are constructed to represent the same N_i and q_i, the ratio is unity for $p = 0$ and $p = 3$. By definition, the ratio is also unity for $v = 0$. For any positive v and p between 0 and 3, the ratio is larger than unity, while for p larger than 3 the ratio is smaller than unity (Figure 3a). Thus, moments three and lower are larger for the gamma distribution than for the exponential, while the opposite is true for higher moments (Figure 9b). The ratio levels off for v larger than 6 or so (Figure 9c).

With respect to the simulations analyzed here, the role of the PSDs stems from dependency of the depositional growth and sublimation rates and sedimentation effects on different moments. The rate of water vapor deposition on ice crystals, being proportional to the first moment of the PSD, increases as the shape parameter v increases and ice spectrum becomes narrower for given N_i and q_i. Indeed, the maximum deposition rate in two models using an effective $v = 2$ in calculation of the deposition rate (COSMO and UCLALES-SB) is larger than in models that assume an exponential distribution (DHARMA-2M, SAM-2M, UCLALES, and WRFLES) for comparable values of IWP and N_i (Figure 10). Notably, the two simulations using bin microphysics schemes have a maximum deposition growth rate larger than 2×10^{-5} g m^{-3} s^{-1}, the upper–bound threshold for rapid glaciation of mixed-phase clouds found in *Morrison et al.* [2011], but nevertheless maintain quasi steady state mixed-phase clouds, indicating that other processes also play significant roles and suggesting that the threshold may depend on some microphysical assumptions.
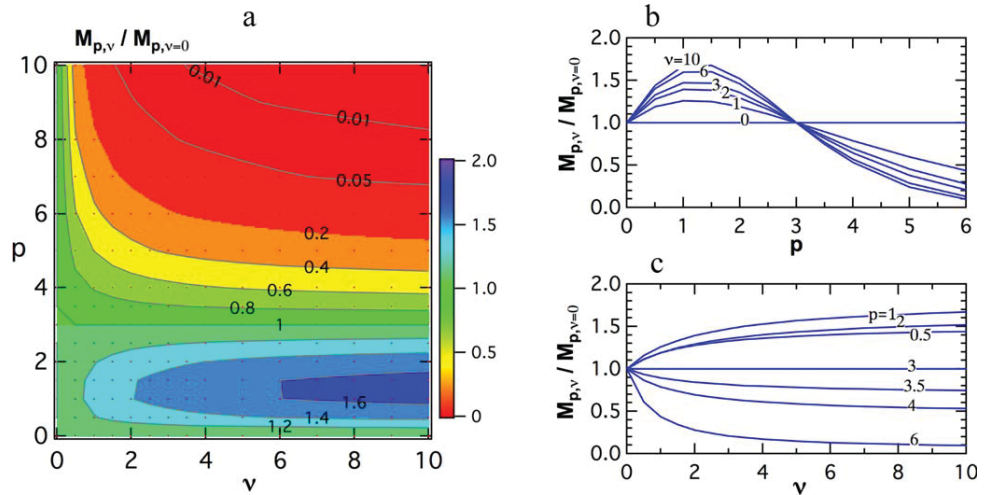
Figure 9. (a) The ratio of the pth moment of gamma ice size distribution with a shape parameter v ($M_{p,v}$) to the pth moment for exponential size distribution ($M_{p,v} = 0$) corresponding to the same ice number concentration and ice water content as a function of p and v. Also shown are the dependencies of the ratio (a) on p for selected v and (c) on v for selected p.

Another important process affected by the shape of the distribution is sedimentation. While the fall speed V_i of an individual ice crystal is prescribed as a function of size ($V_i = a_v D^{0.5}$, where a_v is defined in the Appendix), it is the integral over the size spectrum that is important for the water budget. Furthermore, for any but monodisperse size spectrum, sedimentation affects distributions of mass and number mixing ratios differently. The mass-weighted fall speed (V_{mi}), which controls sedimentation of q_i, is

$$V_{mi} = \frac{a_v \int_0^\infty D^{3.5} \ f(D) dD}{\int_0^\infty D^3 \ f(D) dD}.$$

(10)

Since V_{mi} is proportional to moment 3.5 of the PSD, it is smaller for a gamma distribution with $v = 2$ than for an exponential distribution with the same q_i by about 15% (Figure 9c). Both slower growth rates and faster mass-weighted fall speeds contribute to smaller IWPs predicted by models using exponential ice PSD for ice1 (cf. DHARMA-2M, SAM-2M, UCLALES, and WRFLES in Figure 3c.). For higher ice number concentrations, as in ice4, these models also predict smaller IWP (Figure 3e) than other ensemble members. Models with narrower ice PSDs, such as COSMO and UCLALES-SB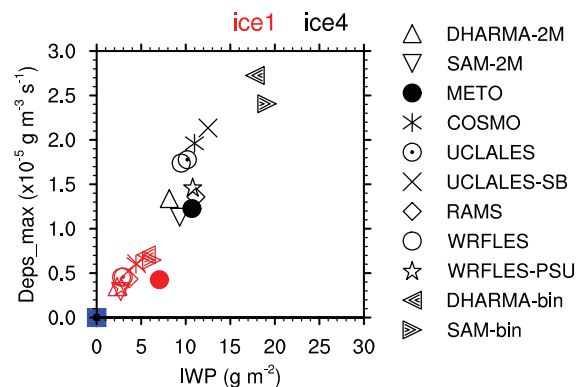 with an effective $v = 2$ in sedimentation calculations, predict stronger precipitation in both ice1 and ice4 runs (Figure 6). In ice4, however, the difference in IWP among different bulk schemes diminishes with time (Figure 3e) as precipitation exceeds the resupply of moisture to the cloud layer from below. For this set of runs, the only two models that result in a significantly higher IWP are models with bin microphysics (DHARMA-bin and SAM-bin).

The number-weighted fall speed for ice particles, which controls sedimentation of N_i, is
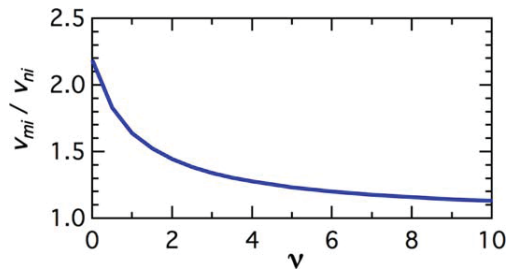

Figure 10. Maximum deposition growth rate of ice particles. Each symbol represents an average value for the last 2 h of simulations. The ice1 runs are shown in red and ice4 in black.

Figure 11. The ratio of the mass-weighted fall speed (V_{mi}) to the number-weighted fall speed (V_{ni}) as a function of the shape parameter of the gamma distribution (v). An exponential distribution used in most bulk models arises when $v = 0$.

$$V_{ni} = \frac{a_v \int_0^\infty D^{0.5}\ f(D)dD}{\int_0^\infty f(D)dD}. \qquad (11)$$

Being controlled by the 0.5th moment of the PSD, the effect of v on V_{ni} is stronger and opposite in sign to the effect on V_{mi} (Figure 9c): V_{ni} for a gamma distribution with $v = 2$, for example, exceeds V_{ni} for an exponential distribution by ~30%.

The ratio V_{mi}/V_{ni}, which indicates the efficiency of size sorting by sedimentation, can be expressed as a function of spectral shape parameter

$$V_{mi}/V_{ni} = \frac{(v+3.5)(v+2.5)(v+1.5)}{[(v+3)(v+2)(v+1)]}. \qquad (12)$$

The dependency of this ratio on v, shown in Figure 11, is stronger than for each of the fall speeds individually because V_{mi} is increasing while V_{ni} is decreasing when v increases. For $v = 0$, the distribution is exponential and $V_{mi}/V_{ni} = 35/16$. Thus, the mass-weighted fall speed for an exponential distribution is about twice the number-weighted fall speed. As v increases and the PSD becomes narrower, the ratio drops off sharply: V_{mi} is higher than V_{ni} by only 40% for $v = 2$ and by 20% for $v = 6$. The decrease slows down for large v, as the ratio approaches the limit of $V_{mi}/V_{ni} = 1$ for a monodisperse spectrum ($v \to \infty$).

4.2. Sensitivity of Simulations to Ice Size Distribution

Given the large sensitivity of bulk process rates to the shape of ice PSD, it is important to understand a realistic range of the shape parameter. One way to obtain this information is through the analysis of simulations conducted using bin microphysics schemes. These schemes do not make assumptions on the shape of the ice size spectrum and explicitly predict the PSDs, notwithstanding uncertainties in the accuracy of these predictions due to assumptions about particle properties, neglect of aggregation in the presented simulations, numerical representations, and other issues. Figure 12 illustrates the variability of the shape parameter in gamma distributions approximating ice size spectra from the DHARMA-bin ice4 simulation, in which v is computed from the relative dispersion of D using the first three moments of the PSD. The domain-average value of v (computed from the domain averages of each of the first three moments) is around 3, but the parameter ranges from 0 to 15 with a pronounced height dependency (Figures 12c and 13). Near the surface, v is small and the ice distributions are nearly exponential. The spectra become narrower with altitude and, in the depositional growth region (between 400 and 800 m levels), v can be 10 or higher with the horizontal mean value of 6 at z = 400 m (Figure 12c). There is no clear correlation between horizontal variability of v and q_c or q_i (Figure 12).

To confirm the role of ice PSD in the evolution of the cloud, sensitivity simulations with altered ice treatments are conducted. Table 3 lists DHARMA and SAM-2M sensitivity experiments, results from which for the ice4 configuration are presented in Figures 14 and 15. Using a gamma ice PSD ($v = 3$) instead of exponential ($v = 0$) in DHARMA-2M simulations leads to a boost in depositional growth rate of ice, a close match of the resulting LWP evolution to that in DHARMA-bin simulations considered as a reference (Figure 14a) and a substantial increase in IWP relative to the default bulk configuration (Figure 14c). Very good agreement in the net longwave radiative flux at the surface, which is determined by LWP in the radiation parameterization, is also achieved with this setup (not shown). The remaining underprediction of IWP in these runs relative to the bin microphysics is presumably because the depositional growth rate is underestimated in the 400–600 m layer, where the spectra in the DHARMA-bin ice4 simulations are narrower ($v \approx 6$, Figure 13b) than those in modified DHARMA-2M ($v = 3$). Analogous experiments with SAM-2M produce similar results. When a narrower gamma ice PSD with $v = 3$ is used instead of the default exponential distribution ($v = 0$), the total condensed water path changes little (Figure 14f), but its partitioning between liquid and ice
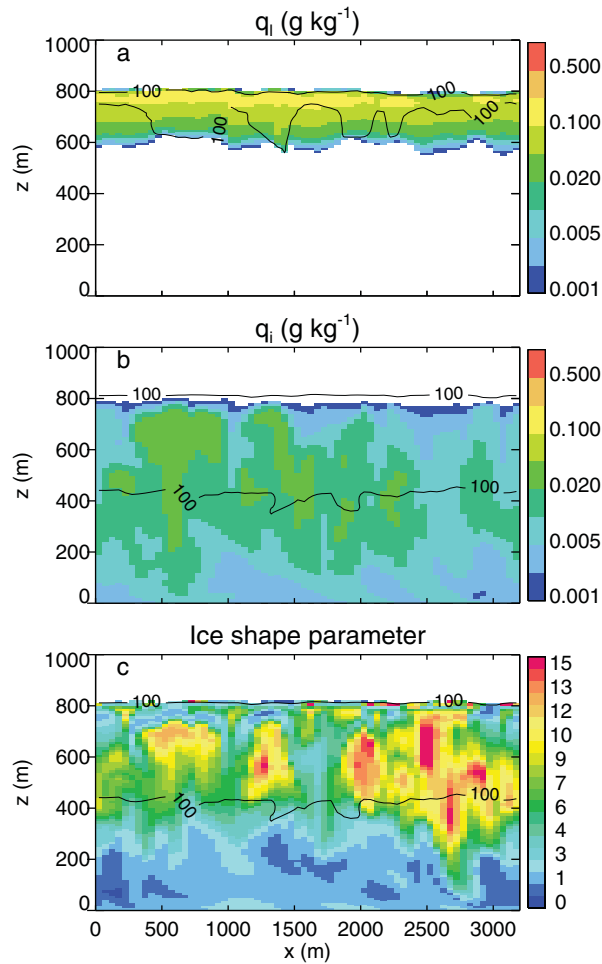
Figure 12. Vertical (x-z) cross sections of (a) liquid (q_c) and (b) ice (q_i) water mixing ratios and (c) the shape parameter (v) for gamma distributions fitted to the predicted ice spectra from the DHARMA-bin ice4 simulation at t = 6 h. Black lines show isolines of 100% relative humidity with respect to liquid (Figure 12a) and ice (Figures 12b and 12c).

phases is altered drastically, bringing both LWP and IWP in much closer agreement with SAM-bin (Figures 14b and 14d). An agreement in precipitation rate is similarly improved (Figures 15a and 15b).

When SAM-2M runs with $v = 0$ and $v = 3$ are repeated with the size-sorting effect turned off by setting $V_{ni} = V_{mi}$, only small changes are seen in LWP, IWP, and precipitation. Although the size-sorting effect in these simulations is small regardless of v, it is only the case because of the constraint on ice concentration imposed in the current setup. When size sorting is turned off, a 70% larger column integrated ice nucleation rate is required to maintain the prescribed N_i in the mixed-phase cloud for $v = 0$ (cf. cases with $v = 0$ and $v = 0$, $V_{ni} = V_{mi}$ in Figure 15a). The effect becomes smaller for larger v because the difference between V_{ni} and V_{mi} is reduced for narrower spectra (Figure 11). Consequently, only a 30% increase in the nucleation rate is needed to offset the size sorting for $v = 3$ (cf. cases with $v = 3$ and $v = 3$, $V_{ni} = V_{mi}$ in Figure 15a). If N_i were to vary and a relatively constant ice nucleation rate were to be prescribed (or predicted), size sorting would have a significant impact on IWP, particularly in models assuming broad (exponential) ice PSDs.

Relative roles of ice PSD effects on LWP and IWP via changes in two processes, namely the crystal fall speed and depositional growth rate, are quantified as follows: Simulations are repeated with a gamma PSD and no size sorting (i.e., $v = 3$, $V_{ni} = V_{mi}$) for one process rate while assuming an exponential PSD in computing the other process rate. The two simulations, Deps($v = 0$) and $V_{mi}(v = 0)$, produce very similar IWPs, which are approximately halfway between those for SAM-bin and SAM-2M. This suggests that accounting for ice PSD is equally important for both processes in order to predict the correct IWP. The LWP evolution, however, is clearly dominated by the size distribution effect on the depositional growth rate as seen in the tight grouping of curves in Figure 14a depending on whether $v = 0$ or $v = 3$ is used in computing the ice crystal growth rate.

To further test the effect of PSD assumptions on ice crystal growth, the parameters of f_m (equation (7)) in COSMO are varied so that the integrated depositional growth rate of ice is reduced to match that in DHARMA-2M and SAM-2M. With this modification, the mean LWP increases, particularly for ice4 (not shown), and COSMO shifts closely toward the cluster of DHARMA-2M, SAM-2M, UCLALES, and WRFLES points in LWP-IWP phase space seen in Figure 7. In another set of runs using COSMO's default scheme, which accounts for ventilation due to the crystals' sedimentation velocity, the depositional growth rate of ice is increased relative to that from intercomparison simulations and liquid water cloud is completely desiccated before the end of the ice4 simulation. In ice1 simulations with ventilation effects, the mean LWP
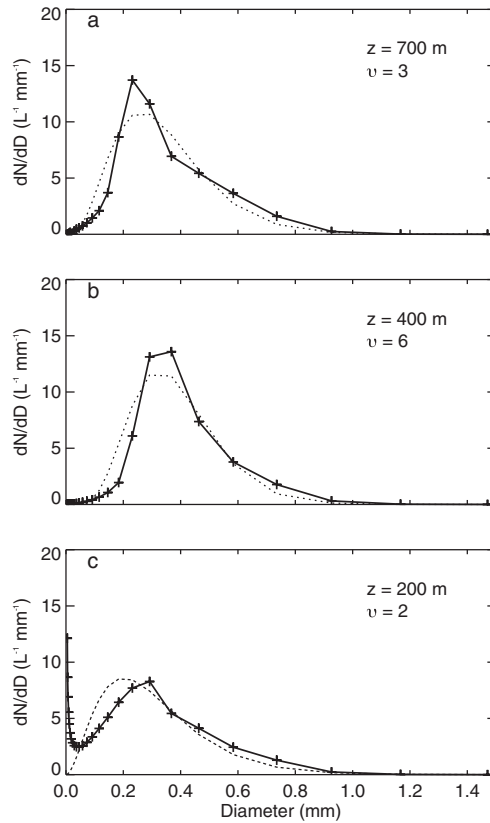
Figure 13. Horizontally averaged ice particle size distribution predicted by the DHARMA-bin ice4 simulation (solid lines) at t = 6 h at three levels: (a) in the middle of the liquid-phase cloud layer (z = 700 m), (b) at the bottom of the depositional growth zone (z = 400 m), and (c) in the middle of the sublimation zone (z = 200 m). Gamma distributions fitted using the first three moments of the size distribution are shown by dotted lines, with corresponding shape parameters v indicated on each plot.

decreases and IWP increases to the point where they are comparable to those from the ice4 run with reduced depositional growth. Thus, the combined effect of a narrow size ice PSD and ventilation is comparable to quadrupling the ice particle concentration with a broader PSD and no ventilation.

4.3. Sublimation Effects on Ice Mass and Number Concentration

According to the microphysics setup, the ice number concentration is essentially fixed within the mixed-phase cloud, i.e., when liquid is also present. In the absence of liquid water, however, ice concentration is allowed to evolve, leading to a significant spread in N_i among the models below the liquid cloud base (Figure 16). One of the main reasons for this is the unconstrained effect of sublimation on N_i. Depositional growth increases q_i but does not affect N_i. This is not necessarily true for sublimation, which can reduce both N_i and q_i, and models use different approaches to account for sublimation-induced reduction in N_i. Five models (DHARMA-2M, SAM-2M, UCLALES, WRFLES, and WRFLES-PSU) assume that sublimation reduces N_i by the same fraction as it reduces q_i, i.e., $(dN_i/N_i)_{sub} = (dq_i/q_i)_{sub}$, or equivalently that the mean ice size is preserved during sublimation. This assumption leads to nearly constant mean ice size below 400 m in these models (Figure 17). In COSMO, UCLALES-SB, and METO, N_i does not change when ice sublimates until the mean ice particle mass falls below a prescribed minimum. That minimum mass is then used to compute updated N_i from q_i after sublimation. When N_i

remains nearly constant as q_i declines throughout the sublimation zone (COSMO, UCLALES-SB, and METO, Figure 18), ice crystals become smaller and fall slower, leading to further decrease in size due to longer exposure to subsaturated conditions. Consequently, these models have the smallest ice particles near the surface (Figure 17). Regional Atmospheric Modeling System (RAMS) employs lookup tables developed from parcel model simulations with bin ice microphysics to obtain $(dN_i/N_i)_{sub}$ from $(dq_i/q_i)_{sub}$ depending on environmental conditions, parameters of the gamma PSD, and ice crystal habit [*Harrington et al.*, 1995].

The effects of these different specifications can be gleaned from comparisons with simulations using bin microphysics schemes, which compute the change in N_i due to sublimation explicitly without invoking additional assumptions and therefore provide a more physically based treatment of the effect of

Table 3. Sensitivity Experiments for the Ice PSD Effects

| Case	Ice PSD Treatment	Model(s)
$v = 0$	Exponential ice PSD, same as default	DHARMA-2M, SAM-2M
$v = 3$	Gamma ice PSD (equation (2)) with $v=3$	DHARMA-2M, SAM-2M
$v = 0, V_{ni} = V_{mi}$	Same as $v = 0$, but no size sorting	SAM-2M
$v = 3, V_{ni} = V_{mi}$	Same as $v = 3$, but no size sorting	SAM-2M
$v = 3, V_{ni} = V_{mi}, V_{mi}(v = 0)$	Same as $v = 3$, but no size sorting and V_{mi} is computed for exponential PSD	SAM-2M
$v = 3, V_{ni} = V_{mi}, Deps(v = 0)$	Same as $v = 3$, but no size sorting and depositional growth is computed for exponential PSD	SAM-2M
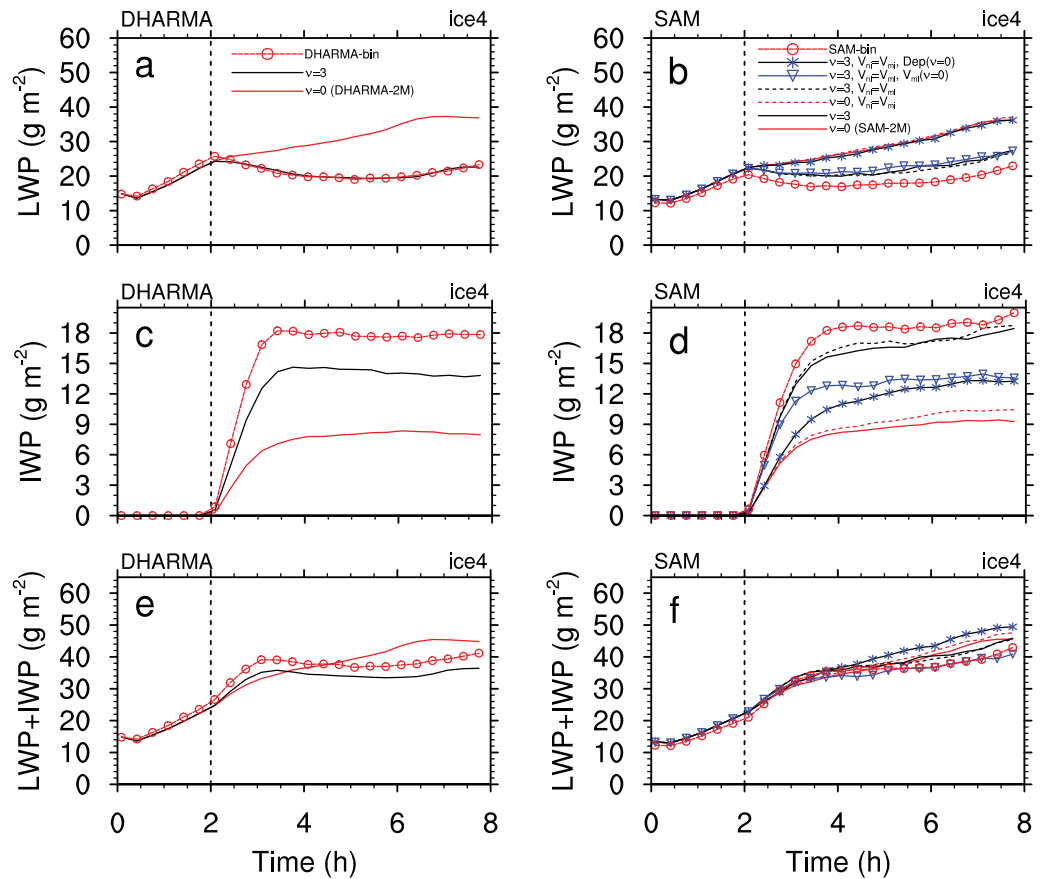
Figure 14. Results of ice particle size distribution sensitivity experiments listed in Table 3. Shown are time evolutions of horizontally averaged (a and b) liquid, (c and d) ice, and (e and f) total condensed water paths for ice4 simulations using DHARMA (Figures 14a, 14c, and 14e) and SAM (Figures 14b, 14d, and 14f). Lines with circles show bin microphysics results from a corresponding model for reference.

sublimation on the parameters of the ice PSD. The bin models show a reduction in both N_i and q_i when precipitating ice particles approach the surface (Figures 16 and 18, DHARMA-bin and SAM-bin), leading to mean crystal size in the sublimation region below 400 m (Figure 17) that is not constant but varies less than in models assuming constant N_i during sublimation.

Note that sedimentation in a sublimation region can lead to an increase in N_i. When sublimation reduces ice particle size and, therefore, V_{ni}, sedimentation leads to convergence of N_i in that layer, which, if not compensated by a sufficient reduction of N_i due to sublimation, will result in a N_i increase, as seen in COSMO, METO, and RAMS profiles in Figure 16.

5. Discussion

What is required for models to realistically simulate persistent mixed-phase Arctic clouds? Results of the intercomparison contribute the following insights to answering this question.

5.1. Dynamics and Liquid Phase Cloud
Liquid-phase cloud properties exert major controls on the dynamics and energetics of the mixed layer in which the cloud resides. Thus, it is critical for the models to produce realistic liquid-phase cloud in order to simulate realistic mixed-phase cloud. The inter-model spread among simulations without ice is found to be comparable to those seen in previous intercomparisons of LES of warm stratocumulus [e.g., *Ackerman et al.*, 2009; *Stevens et al.*, 2005], although specifics of the Arctic environment also provide unique modeling challenges. Arctic mixed layers are often maintained by much weaker turbulence because of a number of potentially seasonally dependent factors, such as smaller LWC, reduced cloud top radiative cooling, small
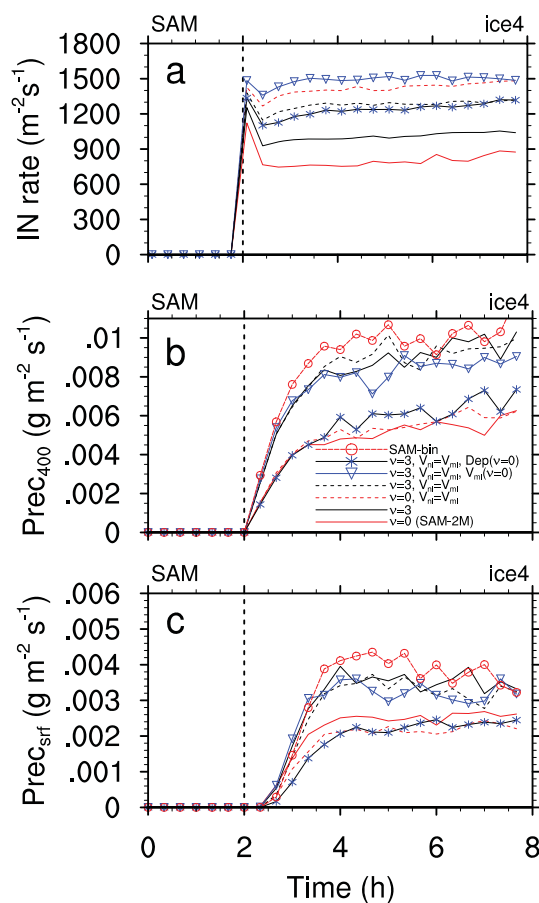
Figure 15. (a) Time evolution of horizontally averaged column-integrated ice nucleation rate and precipitation flux (b) at 400 m level and (c) at the surface for ice4 SAM–2M sensitivity simulations listed in Table 3. The initial ice nucleation rate peak at t = 2 h is omitted for clarity. For Figures 15b and 15c, lines with circles show SAM–bin results for reference.

surface heat fluxes, and periodic decoupling of the cloud containing layer from the surface. Because of the weaker forcing, particularly in the springtime when the Arctic Ocean is still mostly covered with ice as in the considered case, even relatively small changes in cloud dynamics due to cloud ice processes can result in qualitative changes in the liquid-phase cloud and possibly in cloud dissipation. Another complication arises from the fact that the liquid-phase cloud layers in this region are often thin (e.g., 200 m in the considered case) and therefore are difficult to resolve in models having a significantly coarser vertical resolution than the 10 m grid spacing used here.

In this study, Figure 9 demonstrates that inter-model spread in LWP is closely linked with inter-model spread in dynamics, whereas inter-model spread in IWP is independent of inter-model spread in dynamics. Thus, within the constraints of this case (fixed ice properties) and the features of this case (decoupled boundary layer with variable predictions of deepening rate), representation of the liquid-phase and dynamics still present a first-order challenge to models.

5.2. Ice Nucleation

Heterogeneous ice nucleation is one of the most uncertain processes in modeling Arctic mixed-phase clouds. It has been hypothesized that ice multiplication could also be a process that is important to determining ice crystal number concentration. Although the 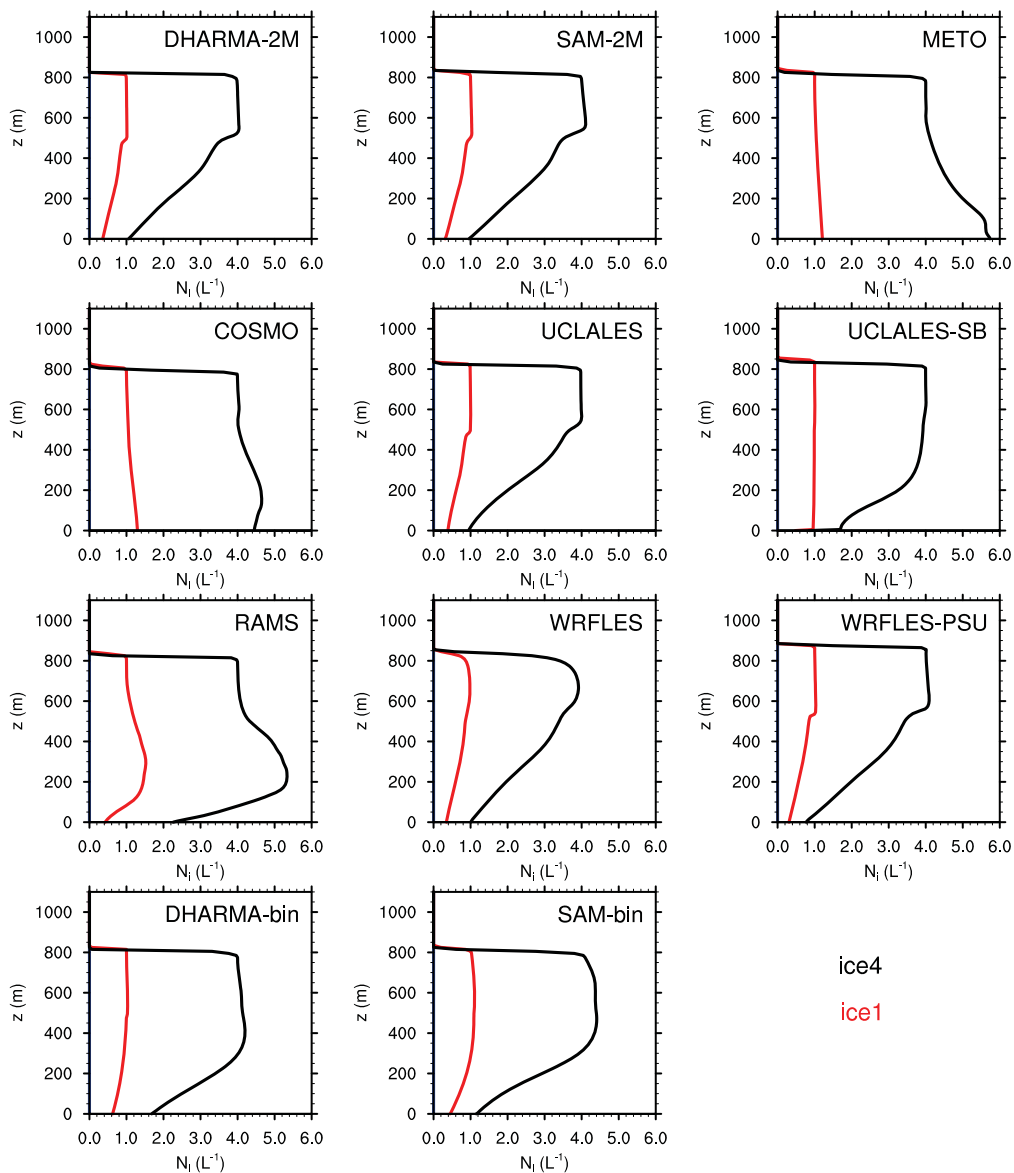simulations analyzed here sidestep the question of how ice crystals form by directly constraining ice number concentration, the presented results still bear important insights.

Simulated clouds demonstrate high sensitivity to the ice crystal number concentration, for which ice nucleation is expected to be the primary controlling factor. At very low ice crystal number concentrations, where desiccation of LWP remains weak, overall cloud evolution may remain weakly affected by the ice. *Fridlind et al.* [2012a] concluded that the observed SHEBA intercomparison case cloud system occurred in this regime, based on analysis of in situ and remote sensing observations. However, if ice crystal number concentration is increased by a relatively modest factor of four or so in either the previous SHEBA or current ISDAC cases, all models indicate a regime of substantial LWP decrease. It is worth noting that the ISDAC case as observed appears likely somewhere between these two extremes, with typically ∼5–20% reduction of LWP over 6 h of simulation time when ice crystal number concentrations are based on observations (Figure 3c). Compared with the commonly days-long lifetime of thin Arctic stratus, such a desiccation rate should be a factor that does limit cloud lifetime and is therefore very important to properly simulate in climate models. In contrast to these SHEBA and ISDAC cases over ice surfaces, autumnal cold-air-outbreak cloud systems over ice-free ocean, such as the MPACE intercomparison case, would be more resilient to variations in ice number concentration owing to high surface heat and moisture fluxes.

Overall, improving representation of ice nucleation clearly remains a first-order problem in modeling mixed-phase clouds because when the high sensitivity of cloud macrostructure to ice concentration is

Figure 16. Domain-mean profiles of ice number concentration from all the models. The profiles are averaged over the last 2 h of simulations. The ice1 runs are shown in red and ice4 in black.

combined with a large uncertainty in ice nucleation rates from various available parameterizations, models cannot reliably predict whether clouds will persist for a long time or glaciate and dissipate quickly. Additional observations and analysis will be needed to establish in what sensitivity regime range mixed-phase Arctic clouds most commonly occur and why.

5.3. Number and Mass Precipitation Fluxes

In a steady state cloud, neglecting aggregation, the net flux of ice particles through the cloud base is balanced by the ice formation rate integrated through the cloudy column above, and the net ice mass flux is equal to the deposition growth rate of ice crystals integrated through the same column [*Westbrook and Illingworth*, 2013]. An ultimate goal for simulations of ice-containing clouds is to correctly reproduce number and mass fluxes simultaneously.

Ice mass flux controls the effect of ice processes on the energy and water balance of the cloud layer. Considering a cloud in a steady state, the ice number flux is determined by the ice nucleation rate and crystal
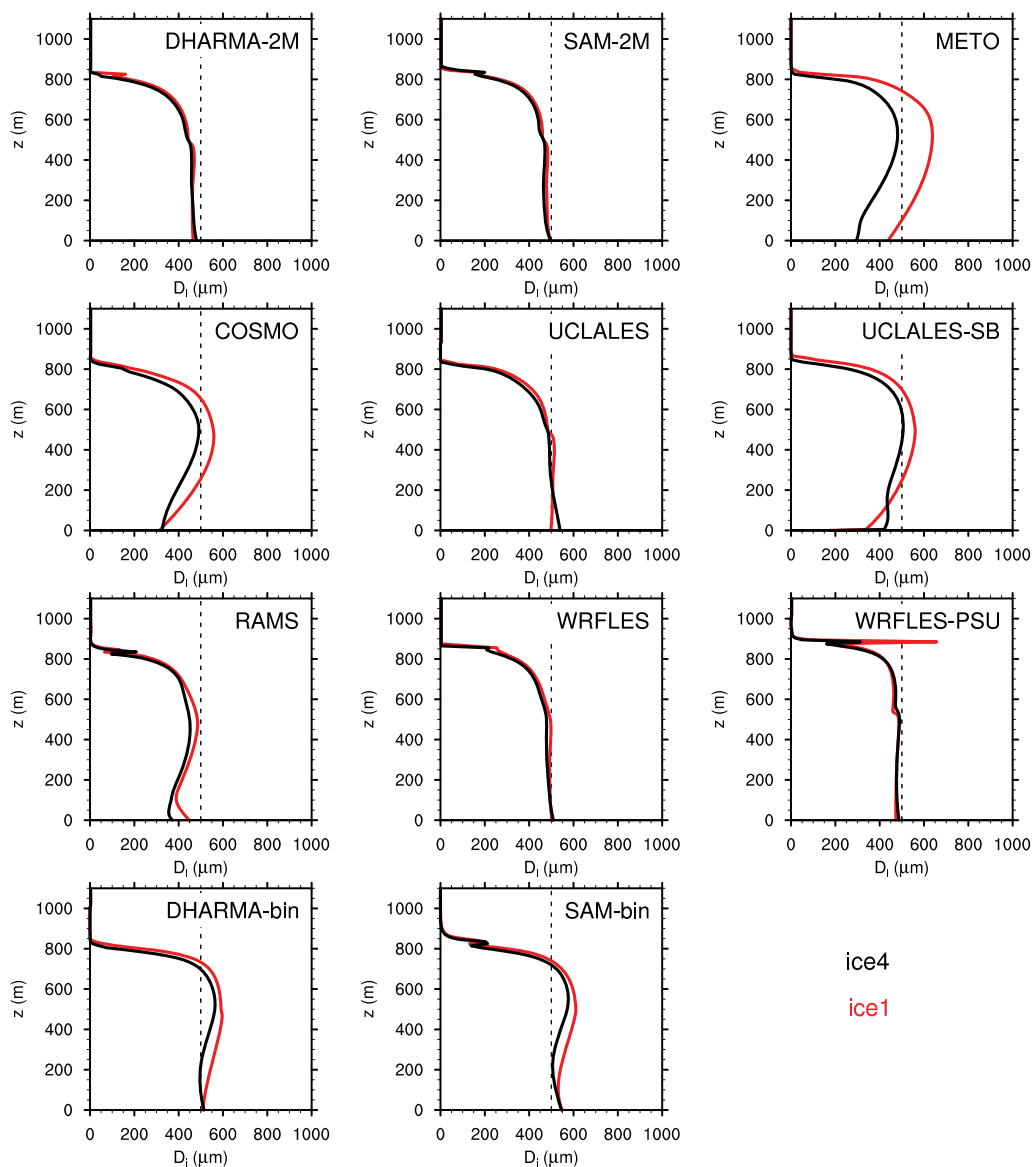
Figure 17. Domain-mean profiles of mass mean diameter of ice particles from all the models. The profiles are averaged over the last 2 h of simulations. The ice1 runs are shown in red and ice4 in black. Dashed vertical line marks 500 μm diameter for reference.

growth rate [*Yang et al.*, 2013] and predicting it correctly is critical for studies of aerosol effects on cold clouds. If the number flux is over (under)-estimated, then a given nucleation rate would result in lower (higher) in-cloud ice concentration. Alternatively, in simulations aimed at reproducing an observed ice concentration, models that over (under)-predict ice particle number flux out of the cloud would require higher (lower) ice nucleation rate.

Number and mass precipitation fluxes are intrinsically related via the ice PSD. The results presented in this paper imply that the exponential ice PSD may be inadequate in representing ice size spectra over the entire domain. It must be kept in mind that this study has not considered processes of aggregation or riming of ice crystals, which may further complicate the evolution of ice particle spectra.

It is noteworthy that another important factor for both mass and number fluxes is intentionally sidestepped in this study: ice particle properties. Indeed they are specified here for the first time in a intercomparison study in order to remove a model-to-model difference to which results are known to be sensitive [*Avramov*
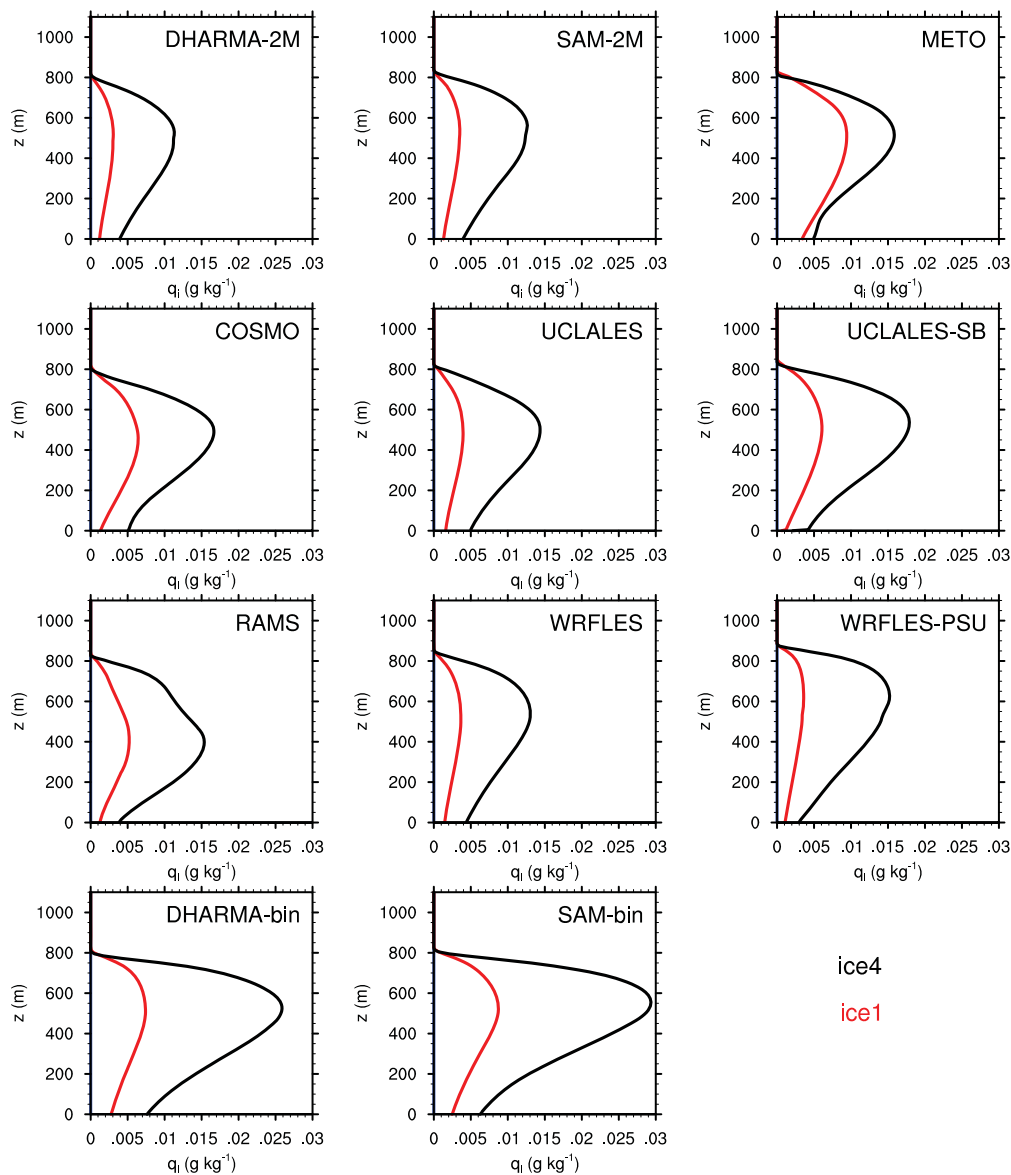
Figure 18. Domain-mean profiles of ice mixing ratio from all the models. The profiles are averaged over the last 2 h of simulations. The ice1 runs are shown in red and ice4 in black.

and Harrington, 2010]. As in the case of ice nucleation, it is not possible to base the specification on measurements of ice crystal properties because current instruments unfortunately provide insufficient information to constrain models [cf. *Fridlind et al.*, 2012a].

6. Summary and Conclusions

Results from large-eddy simulations of mixed-phase Arctic clouds by 11 different model configurations are analyzed with the goal of improving understanding and model representation of processes controlling the evolution of these clouds. The considered case is based on a long-lived mixed-phase cloud observed on 26 April 2008 during ISDAC. Sensitivity of the simulated cloud properties to the prescribed in-cloud ice particle concentration (N_i) is analyzed. It is found that N_i exerts significant influence on the cloud structure when increasing N_i leads to a substantially reduced LWP and potential cloud dissipation, in agreement with earlier

studies [e.g., *Fan et al.*, 2009; *Klein et al.*, 2009; *Morrison et al.*, 2011; *Ovchinnikov et al.*, 2011; *Pinto*, 1998; *Rauber and Tokay*, 1991; *Solomon et al.*, 2009]. This reaffirms previous conclusions that development of accurate ice nucleation parameterizations remains a first-order priority in modeling of this cloud type, especially in studies concerning aerosol effects on clouds.

Based on identification of likely sources of rather extreme model divergence in previous intercomparisons of mixed-phase cloud simulations [*Klein et al.*, 2009; *Morrison et al.*, 2011], all models in this study use the same single-particle properties (i.e., mass-size, mass-fall speed, and mass-capacitance relationships). Using a semi-idealized setup, simulations with constrained properties of individual ice particles expose the role of ice crystal PSDs in influencing cloud evolution. A clear separation in cloud liquid and ice water paths predicted by models with bin (size resolved) and bulk microphysical treatments is documented. Considering that all models employ the same single-particle properties (in addition to identical spatial resolution, surface fluxes, radiation parameterization, nudging specifications, etc.), the spread in predicted LWP and IWP is quite remarkable (Figures 3 and 8). The presented analysis suggests that much of that variability can be attributed to the treatment of the ice particle spectrum. Indeed, grouping of models using the same parameterizations of ice PSD is clearly seen, especially for ice4 simulations (note the clustering of COSMO and UCLALES-SB; DHARMA-bin and SAM-bin; and DHARMA-2M, SAM-2M, UCLALES, and WRFLES in Figure 8). These differences in ice PSD appear more important to predicted IWP than either dynamics or LWP, explaining the independence of IWP inter-model spread from LWP and dynamics inter-model spread in Figures 7 and 8, as well as the model groupings of predicted IWP.

These results strongly suggest that in both interpreting simulations and developing new parameterizations for ice microphysics more attention should be paid to representation of the ice particle size spectrum in addition to formulations of ice nucleation and single-particle properties, the two aspects that are often considered as dominant sources of uncertainty in mixed-phase cloud modeling. The assumed relative width of the ice PSD used in many two-moment schemes strongly affects bulk sedimentation, depositional growth and sublimation rates. Simulations using bin microphysics suggest that an exponential ice PSD, a common default choice of many bulk schemes, is too broad and results in underestimation of vapor deposition rate and overestimation of mass-weighted ice fall speed, which together lead to an underprediction of ice water path by a factor of two or more in the case investigated. An exponential distribution also results in accelerated removal via sedimentation of ice mass concentration relative to the number concentration, which leads to an underestimation of ice crystal size in the cloud. Adjusting the ice spectrum shape parameter in bulk schemes can significantly reduce these inter-model differences and bring the cloud structure predicted by bulk schemes into closer agreement with bin models. However, the "fix" demonstrated here requires a priori knowledge of the target ice spectrum shape, which in nature is expected to vary. A robust solution to the problem is through the development of a method to predict or diagnose a measure of the relative width of the ice spectrum using a combination of in situ and remote sensing observations and modeling [*Milbrandt and Yau*, 2005]. Ongoing and new efforts in this direction should be encouraged.

Appendix A: Simulation Setup

A1. Initial Atmospheric Profiles
Initial profiles of temperature, moisture, and horizontal wind components are based on aircraft observations in the mixed layer and idealization of a sounding at Barrow, AK.

The initial liquid water potential temperature profile, $\theta_{l,0}$, is given by

$$\theta_{l,0}(z) = \begin{cases} 265 + 0.004 \cdot (z\text{-}400) & [K], & z < 400\,\text{m} \\ 265 & [K], & 400\,\text{m} \leq z < 825\,\text{m} \\ 266 + (z\text{-}825)^{0.3} & [K], & 825\,\text{m} \leq z < 2045\,\text{m} \\ 271 + (z\text{-}2000)^{0.33} & [K], & z \geq 2045\,\text{m} \end{cases} \tag{A1}$$

and the initial total water mixing ratio, $q_{t,0}$, is

$$q_{t,0}(z) = \begin{cases} 1.5 - 0.00075 \cdot (z\text{-}400) & [\text{g/K}], \quad z < 400\,\text{m} \\ 1.5 & [\text{g/K}], \quad 400\,\text{m} \le z < 825 \\ 1.2 & [\text{g/K}], \quad 825\,\text{m} \le z < 2045\,\text{m} \\ 0.5 - 0.000075 \cdot (z\text{-}2045) & [\text{g/K}], \quad z \ge 2045\,\text{m} \end{cases} \tag{A2}$$

Zonal, U_0, and meridional, V_0, wind components are specified as

$$\begin{aligned} U_0(z) &= -7 & [\text{m s}^{-1}], \\ V_0(z) &= -2 + 0.003 \cdot z & [\text{m s}^{-1}]. \end{aligned} \tag{A3}$$

In the expressions (A1–A3) and throughout this document, z is the altitude above the ice-covered ocean in meters.

The specified initial moisture profile contains a cloud layer, i.e., a layer that is supersaturated with respect to liquid water. Models with bulk microphysics diagnose the condensed water from the saturation adjustment immediately at the beginning of a simulation. Schemes that use bin microphysics compute the condensation rate explicitly produce cloud water more gradually.

The initial temperature is perturbed below the top of the mixed layer ($z < 825$ m) with pseudorandom fluctuations with amplitude of 0.1 K. In models in which the subgrid turbulent kinetic energy (TKE) is a prognostic variable it is initialized at 0.1 m^2 s^{-2}.

A2. Surface

Sensible and latent heat fluxes between ice covered ocean and the atmosphere under the considered conditions are typically small ($\sim$10 W m^{-2}). Furthermore, since during ISDAC F31 the mixed layer in which the cloud resides initially does not extend to the surface, the effect of these fluxes on the cloud layer is reduced even further. Thus, for simplicity, both sensible and latent surface heat fluxes are set to zero in these simulations.

Surface pressure is set to 1020 hPa and surface roughness length is 4×10^{-4} m.

A3. Large-Scale Forcing

Large-scale subsidence is specified by integrating the prescribed horizontal wind divergence upward from the surface. The divergence is assumed to be constant below the inversion and zero above:

$$D = \begin{cases} 5 \cdot 10^{-6} & [\text{s}^{-1}], \quad z < 825\,\text{m} \\ 0 & [\text{s}^{-1}], \quad 825\,\text{m} \le z \end{cases} \tag{A4}$$

This gives a linear increase in the large-scale subsidence from zero at the surface to 0.4125 cm s^{-1} at the base of the initial inversion (z = 825 m), above which the large-scale vertical wind w_{LS} is constant:

$$w_{\text{LS}} = \begin{cases} -5 \cdot 10^{-6}\,z & [\text{m s}^{-1}], \quad z < 825\,\text{m} \\ -0.412510^{-2} & [\text{m s}^{-1}], \quad 825\,\text{m} \le z \end{cases} \tag{A5}$$

Large-scale subsidence is accounted for via a source term for any prognostic variable ϕ (other than wind components) in the form $-w_{\text{LS}}(\partial\phi/\partial z)$.

Nudging of the horizontal wind components, temperature and moisture profiles is performed by adding a source term $-c_\phi \, [\phi(z)\text{-}\phi_0(z)] \, \Delta t$ to the prognostic equations for $\phi\{\theta_l,\, q_t,\, U,\, \text{and}\, V\}$. Here $\phi(z)$ is the domain-mean profile, $\phi_0(z)$ denotes the initial profiles of a considered quantity, and Δt is the model time step. Nudging coefficients are specified to have the height dependency in the form

$$c_{\theta,qt}(z) = \begin{cases} 0, & [s^{-1}], \quad z < z_1 = 1200\,\text{m} \\ 1/3600 \cdot \{1\text{-cos}\,[\pi \cdot (z\text{-}z_1)/(z_2\text{-}z_1)]\}/2 & [s^{-1}], \quad z_1 \le z \le z_2 = 1500\,\text{m} \\ 1/3600, & [s^{-1}], \quad z > z_2 \end{cases}$$

$$c_{U,V}(z) = \begin{cases} 1/7200 \cdot [1\text{-cos}\,(\pi \cdot z/z_{UV})]/2 & [s^{-1}], \quad z \le z_{UV} = 825\,\text{m} \\ \\ 1/7200, & [s^{-1}], \quad z > z_{UV} \end{cases}$$

A4. Radiation

In order to minimize inter-model differences due to radiative transfer codes, longwave radiative cooling is parameterized using an approach adopted in several previous GCSS intercomparison projects [e.g., *Stevens et al.*, 2005; *Ackerman et al.*, 2009] and evaluated in *Larson et al.* [2007]. In this scheme, the net upward longwave radiative flux F is computed as a function of liquid water mixing ratio profile. Thus

$$F(z) = F_0 \exp\left(-k[LWP(z_t) - LWP(z)]\right) + F_1 \exp\left(-kLWP(z)\right), \tag{A6}$$

where LWP is the liquid water path between the surface and a level z

$$LWP(z) = \int_0^z \rho(z') q_l(z') dz', \tag{A7}$$

ρ is air density, q_l is the cloud water mixing ratio, and F_0, F_1, and k are tuning parameters. F_0 and F_1 can be interpreted as the net radiative fluxes above and below an optically thick cloud layer. These fluxes drive the radiative cooling below the cloud top and heating above the cloud base. Absorptivity is represented by k. From (A6) the heating rate is obtained

$$\left(\frac{\partial T}{\partial t}\right)_{LWrad} = -\frac{1}{\rho c_p}\frac{\partial F}{\partial z}. \tag{A8}$$

Note that *Stevens et al.* [2005] and *Ackerman et al.* [2009] included a third term in the right-hand side of (A6) to provide extra cooling to compensate subsidence-induced warming and preserve the initial temperature profile above the cloud. The term is not used in the setup presented here. Instead temperature and moisture fields above 1200 m level are nudged toward the initial value as described earlier.

Parameters F_0, F_1, and k are adjusted, so the parameterized heating rate profiles match closely those computed using the Rapid Radiative Transfer Model (RRTM) [*Clough et al.*, 2005; *Iacono et al.*, 2008]. The parameters are given in Table A1. The root-mean-square errors of the heating rate profiles obtained using these fits are on the order of 10^{-5} K s^{-1} ($\sim$0.04 K h^{-1}).

The effect of solar radiation is neglected in all simulations.

A5. Ice growth Processes and Ice Sedimentation

Ice properties are constrained on a single particle basis. In size-resolved (bin) schemes, these properties can be implemented directly. In bulk schemes, the consistency among models may not be fully preserved due to differences in underlying assumptions about the ice PSD, but using the same single particle relationships is expected to reduce the uncertainty among these treatments as well.

In computing the depositional growth rate for an ice particle, the ventilation and radiation effects are neglected. Thus, the mass growth rate is written as

$$\frac{dm_i}{dt} = 4\pi BCS_i, \tag{A9}$$

Table A1. Parameters of the Radiation Scheme

Parameter	F_0 (W m^{-2})	F_1 (W m^{-2})	κ (m^2 kg^{-1})
Value	72	15	170

where C is the capacitance (a measure acting as an effective radius for nonspherical particles), S_i is the fractional supersaturation of water vapor with respect to ice $S_i = \frac{e}{e_{s,i}} - 1$, e is the ambient vapor pressure, $e_{s,i}$ is the saturation vapor pressure over plane ice surface, and B is given by [e.g., *Rogers and Yau*, 1989, equation 9.4]

$$B = \frac{1}{\frac{R_v T}{e_{s,i} D_v} + \frac{L_s}{KT}\left(\frac{L_s}{R_v T} - 1\right)}.$$
(A10)

Here R_v is the gas constant for water vapor, T is temperature, D_v is the coefficient of diffusivity of water vapor in air, L_s is latent heat of sublimation, and K is the coefficient of air heat conductivity.

In order to integrate (A9) in time, a relation between C and m must be specified. We relate capacitance and mass using a power law fit to observations of free falling crystals growing under water saturated conditions at $T_c = -12.2°C$ as reported by *Takahashi et al.* [1991] and recently reanalyzed by *Westbrook and Heymsfield* [2011]

$$C = a_c \, m_i^{b_c},$$
(A11)

where $a_c = 0.09$ m kg$^{-b_c}$ and $b_c = 1/3$. Here and in all power laws to follow MKS units are used. The capacitance and the maximum particle dimension (D) are related via $D = \pi C$. Mass as a function of D can be obtained by inverting (A11) to yield

$$m_i = a_m \, D^{b_m},$$
(A12)

where $a_m = 44.2$ kg m$^{-b_m}$ and $b_m = 3$. The fall speed (V_i) is given by

$$V_i = a_V \, D^{b_V},$$
(A13)

where $a_V = 12$ m$^{1-b_V}$ s^{-1} and $b_V = 0.5$.

The initial size of newly nucleated ice crystals is set to $D = 10$ μm in bulk models or specified as the smallest allowable size in the bin models.

The ice properties formulated above represent an idealization of dendrites as spheres of constant and low equivalent density. While this approximation addresses the goals of this intercomparison, it does not account for changing aspect ratio often occurring in growing crystals [*Sulia and Harrington*, 2011].

A6. Other Parameters

Latitude is 71.32° and longitude is −156.61°.

Surface skin temperature is 267 K.

The period of simulation is from 18:00Z 26 April to 02:00Z 27 April 2008.

References

Ackerman, A. S., et al. (2009), Large-eddy simulations of a drizzling, stratocumulus-topped marine boundary layer, *Mon. Weather Rev.*, *137*(3), 1083–1110, doi:10.1175/2008mwr2582.1.

Avramov, A., and J. Y. Harrington (2010), Influence of parameterized ice habit on simulated mixed phase Arctic clouds, *J. Geophys. Res.*, *115*, D03205, doi:10.1029/2009jd012108.

Avramov, A., et al. (2011), Toward ice formation closure in Arctic mixed-phase boundary layer clouds during ISDAC, *J. Geophys. Res.*, *116*, D00T08, doi:10.1029/2011jd015910.

Clough, S. A., M. W. Shephard, E. Mlawer, J. S. Delamere, M. Iacono, K. Cady-Pereira, S. Boukabara, and P. D. Brown (2005), Atmospheric radiative transfer modeling: A summary of the AER codes, *J. Quant. Spectrosc. Radiat. Transfer*, *91*(2), 233–244, doi:10.1016/j.jqsrt.2004.05.058.

Comstock, K. K., R. Wood, S. E. Yuter, and C. S. Bretherton (2004), Reflectivity and rain rate in and below drizzling stratocumulus, *Q. J. R. Meteorol. Soc.*, *130*(603), 2891–2918, doi:10.1256/qj.03.187.

Cotton, W. R., et al. (2003), RAMS 2001: Current status and future directions, *Meteorol. Atmos. Phys.*, *82*(1-4), 5–29, doi:10.1007/s00703-001-0584-9.

DeMott, P. J., A. J. Prenni, X. Liu, S. M. Kreidenweis, M. D. Petters, C. H. Twohy, M. S. Richardson, T. Eidhammer, and D. C. Rogers (2010), Predicting global atmospheric ice nuclei distributions and their impacts on climate, *Proc. Natl. Acad. Sci. U. S. A.*, *107*(25), 11217–11222, doi:10.1073/pnas.0910818107.

Earle, M. E., P. S. K. Liu, J. W. Strapp, A. Zelenyuk, D. Imre, G. M. McFarquhar, N. C. Shantz, and W. R. Leaitch (2011), Factors influencing the microphysics and radiative properties of liquid-dominated Arctic clouds: Insight from observations of aerosol and clouds during ISDAC, *J. Geophys. Res.*, *116*, D00T09, doi:10.1029/2011JD015887.

Fan, J., M. Ovtchinnikov, J. M. Comstock, S. A. McFarlane, and A. Khain (2009), Ice formation in Arctic mixed-phase clouds: Insights from a 3-D cloud-resolving model with size-resolved aerosol and cloud microphysics, *J. Geophys. Res.*, *114*, D04205, doi:10.1029/2008JD010782.

Fan, J., S. Ghan, M. Ovchinnikov, X. Liu, P. J. Rasch, and A. Korolev (2011), Representation of Arctic mixed-phase clouds and the Wegener-Bergeron-Findeisen process in climate models: Perspectives from a cloud-resolving study, *J. Geophys. Res.*, *116*, D04205, doi:10.1029/2010JD015375.

Ferrier, B. S. (1994), A double-moment multiple-phase 4-class bulk ice scheme. 1. Description, *J. Atmos. Sci.*, *51*(2), 249–280.

Fridlind, A. M., et al. (2012a), A comparison of TWP-ICE observational data with cloud-resolving model results, *J. Geophys. Res.*, *117*, D05204, doi:10.1029/2011jd016595.

Fridlind, A. M., B. van Diedenhoven, A. S. Ackerman, A. Avramov, A. Mrowiec, H. Morrison, P. Zuidema, and M. D. Shupe (2012b), A FIRE-ACE/SHEBA case study of mixed-phase arctic boundary layer clouds: Entrainment rate limitations on rapid primary ice nucleation processes, *J. Atmos. Sci.*, *69*(1), 365–389, doi:10.1175/jas-d-11–052.1.

Harrington, J. Y., M. P. Meyers, R. L. Walko, and W. R. Cotton (1995), Parameterization of ice crystal conversion processes due to vapor deposition for mesoscale models using double-moment basis functions. 1. Basic formulation and parcel model results, *J. Atmos. Sci.*, *52*(23), 4344–4366, doi:10.1175/1520-0469.

Hoose, C., and O. Möhler (2012), Heterogeneous ice nucleation on atmospheric aerosols: A review of results from laboratory experiments, *Atmos. Chem. Phys.*, *12*(20), 9817–9854, doi:10.5194/acp-12–9817-2012.

Iacono, M. J., J. S. Delamere, E. J. Mlawer, M. W. Shephard, S. A. Clough, and W. D. Collins (2008), Radiative forcing by long-lived greenhouse gases: Calculations with the AER radiative transfer models, *J. Geophys. Res.*, *113*, D13103, doi:10.1029/2008jd009944.

Jackson, R. C., G. M. McFarquhar, A. V. Korolev, M. E. Earle, P. S. K. Liu, R. P. Lawson, S. Brooks, M. Wolde, A. Laskin, and M. Freer (2012), The dependence of ice microphysics on aerosol concentration in arctic mixed-phase stratus clouds during ISDAC and M-PACE, *J. Geophys. Res.*, *117*, D15207, doi:10.1029/2012jd017668.

Khain, A., A. Pokrovsky, M. Pinsky, A. Seifert, and V. Phillips (2004), Simulation of effects of atmospheric aerosols on deep turbulent convective clouds using a spectral microphysics mixed-phase cumulus cloud model. Part I: Model description and possible applications, *J. Atmos. Sci.*, *61*(24), 2963–2982.

Khairoutdinov, M. F., and D. A. Randall (2003), Cloud resolving modeling of the ARM summer 1997 IOP: Model formulation, results, uncertainties, and sensitivities, *J. Atmos. Sci.*, *60*(4), 607–625.

Klein, S. A., et al. (2009), Intercomparison of model simulations of mixed-phase clouds observed during the ARM Mixed-Phase Arctic Cloud Experiment. I: Single-layer cloud, *Q. J. R. Meteorol. Soc.*, *135*(641), 979–1002, doi:10.1002/Qj.416.

Koop, T. (2013), The seeds of ice in clouds, *Nature*, *498*(7454), 302–302.

Larson, V. E., K. E. Kotenberg, and N. B. Wood (2007), An analytic longwave radiation formula for liquid layer clouds, *Mon. Weather Rev.*, *135*(2), 689–699, doi:10.1175/mwr3315.1.

Lawson, R. P. (2011), Effects of ice particles shattering on the 2D-S probe, *Atmos. Meas. Tech.*, *4*(7), 1361–1381, doi:10.5194/amt-4-1361-2011.

McFarquhar, G. M., et al. (2011), Indirect and semi-direct aerosol campaign the impact of Arctic aerosols on clouds, *Bull. Am. Meteorol. Soc.*, *92*(2), 183–201, doi:10.1175/2010BAMS2935.1.

Meyers, M. P., R. L. Walko, J. Y. Harrington, and W. R. Cotton (1997), New RAMS cloud microphysics parameterization. 2. The two-moment scheme, *Atmos. Res.*, *45*(1), 3–39.

Milbrandt, J. A., and M. K. Yau (2005), A multimoment bulk microphysics parameterization. Part II: A proposed three-moment closure and scheme description, *J. Atmos. Sci.*, *62*(9), 3065–3081.

Morrison, H., J. A. Curry, and V. I. Khvorostyanov (2005), A new double-moment microphysics parameterization for application in cloud and climate models. Part I: Description, *J. Atmos. Sci.*, *62*(6), 1665–1677.

Morrison, H., et al. (2011), Intercomparison of cloud model simulations of Arctic mixed-phase boundary layer clouds observed during SHEBA/FIRE-ACE, *J. Adv. Model. Earth Syst.*, *3*, M06003, doi:10.1029/2011MS000066.

Morrison, H., G. de Boer, G. Feingold, J. Harrington, M. D. Shupe, and K. Sulia (2012), Resilience of persistent Arctic mixed-phase clouds, *Nat. Geosci.*, *5*(1), 11–17, doi:10.1038/ngeo1332.

Ovchinnikov, M., A. Korolev, and J. Fan (2011), Effects of ice number concentration on dynamics of a shallow mixed-phase stratiform cloud, *J. Geophys. Res.*, *116*, D00T06, doi:10.1029/2011JD015888.

Petty, G. W., and W. Huang (2011), The modified gamma size distribution applied to inhomogeneous and nonspherical particles: Key relationships and conversions, *J. Atmos. Sci.*, *68*(7), 1460–1473, doi:10.1175/2011jas3645.1.

Pinto, J. O. (1998), Autumnal mixed-phase cloudy boundary layers in the Arctic, *J. Atmos. Sci.*, *55*(11), 2016–2038.

Rauber, R. M., and A. Tokay (1991), An explanation for the existence of supercooled water at the top of cold clouds, *J. Atmos. Sci.*, *48*(8), 1005–1023.

Rogers, R. R., and M. K. Yau (1989), *A Short Course in Cloud Physics*, 3rd ed., 293 pp., Pergamon Press, Oxford, U.K.

Seifert, A., and K. D. Beheng (2006), A two-moment cloud microphysics parameterization for mixed-phase clouds. Part 1: Model description, *Meteorol. Atmos. Phys.*, *92*(1-2), 45–66, doi:10.1007/s00703-005-0112-4.

Shutts, G. J., and M. E. B. Gray (1994), A numerical modeling study of the geostrophic adjustment process following deep convection, *Q. J. R. Meteorol. Soc.*, *120*(519), 1145–1178, doi:10.1002/qj.49712051903.

Solomon, A., H. Morrison, O. Persson, M. D. Shupe, and J. W. Bao (2009), Investigation of microphysical parameterizations of snow and ice in Arctic clouds during M-PACE through model-observation comparisons, *Mon. Weather Rev.*, *137*(9), 3110–3128, doi:10.1175/2009mwr2688.1.

Stevens, B., et al. (2005), Evaluation of large-Eddy simulations via observations of nocturnal marine stratocumulus, *Mon. Weather Rev.*, *133*(6), 1443–1462.

Sulia, K. J., and J. Y. Harrington (2011), Ice aspect ratio influences on mixed-phase clouds: Impacts on phase partitioning in parcel models, *J. Geophys. Res.*, *116*, D21309, doi:10.1029/2011jd016298.

Takahashi, T., T. Endoh, G. Wakahama, and N. Fukuta (1991), Vapor diffusional growth of free-falling snow crystals between −3 and −23°C, *J. Meteorol. Soc. Jpn.*, *69*(1), 15–30.

Uttal, T., et al. (2002), Surface heat budget of the Arctic Ocean, *Bull. Am. Meteorol. Soc.*, *83*(2), 255–275.

Verlinde, J., et al. (2007), The mixed-phase Arctic cloud experiment, *Bull. Am. Meteorol. Soc.*, *88*(2), 205–221, doi:10.1175/Bams-88-2-205.

Vogel, B., H. Vogel, D. Bäumer, M. Bangert, K. Lundgren, R. Rinke, and T. Stanelle (2009), The comprehensive model system COSMO-ART—Radiative impact of aerosol on the state of the atmosphere on the regional scale, *Atmos. Chem. Phys.*, *9*(22), 8661–8680.

Westbrook, C. D., and A. J. Heymsfield (2011), Ice crystals growing from vapor in supercooled clouds between −2.5° and −22°C: Testing current parameterization methods using laboratory data, *J. Atmos. Sci.*, *68*(10), 2416–2429, doi:10.1175/jas-d-11–017.1.

Westbrook, C. D., and A. J. Illingworth (2013), The formation of ice in a long-lived supercooled layer cloud, *Q. J. R. Meteorol. Soc.*, *139*(677), 2209–2221, doi:10.1002/qj.2096.

Yamaguchi, T., and G. Feingold (2012), Technical note: Large-eddy simulation of cloudy boundary layer with the Advanced Research WRF model, *J. Adv. Model. Earth Syst.*, *4*, M09003, doi:10.1029/2012ms000164.

Yang, F., M. Ovchinnikov, and R. A. Shaw (2013), Minimalist model of ice microphysics in mixed-phase stratiform clouds, *Geophys. Res. Lett.*, *40*, 3756–3760, doi:10.1002/grl.50700.

Zelenyuk, A., D. Imre, M. Earle, R. Easter, A. Korolev, R. Leaitch, P. Liu, A. M. Macdonald, M. Ovchinnikov, and W. Strapp (2010), In situ characterization of cloud condensation nuclei, interstitial, and background particles using the single particle mass spectrometer, SPLAT II, *Anal. Chem.*, *82*(19), 7943–7951, doi:10.1021/Ac1013892.